Hydromechanical modelling of the influence of water saturation on the penetration performance of concrete target

Yun Jia, Yudan Jin, Hanbing Bian, Wei Wang, Jianfu Shao

Engineering Structures 316 (2024) 118563

Contents lists available at ScienceDirect

Engineering Structures

journal homepage: www.elsevier.com/locate/engstruct

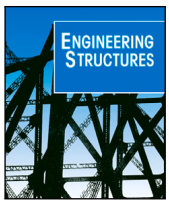

Hydromechanical modelling of the influence of water saturation on the penetration performance of concrete target

Yun Jia [a], Yudan Jin [b], Hanbing Bian [c,*], Wei Wang [d], Jianfu Shao [a]

[a] Univ. Lille, CNRS, Centrale Lille, UMR 9013 - LaMcube - Laboratoire de Mécanique, Multiphysique, Multi-échelle, F-59000 Lille, France
[b] Univ Orléans, Univ Tours, INSA CVL, EA 7494 - Lamé - Laboratoire de Mécanique Gabriel Lamé, F-45000 Orléans, France
[c] Univ. Lille, -LGCgE- Laboratoire de Génie Civil et géo-Environnement, F-59000 Lille, France
[d] College of Civil and Transportation Engineering, Hohai University, Nanjing 210098, China

ARTICLE INFO

Keywords:
Water saturation
Interstitial pressure
Hydro-mechanical behaviour
Elastoplasticity
Concrete
Penetration performance

ABSTRACT

The objective of the present paper is to study numerically the hydro-mechanical behaviour of concrete targets subjected to a rigid projectile, with special attention to the influence of water saturation. An elastoplastic model, encompassing two primary plastic mechanisms (shear and pore collapse), is improved to capture the influence of water saturation. The adopted model is implemented in the finite element code Abaqus/Explicit and validated by simulating two dynamic compression tests at the material point level and two penetration tests at the structure level. Not only a strong influence of water saturation on both volumetric and deviatoric behaviours of concrete is observed at material point level, but also the time-evolutions of projectile velocity, projectile deceleration and penetration depth in concrete targets are also satisfactorily reproduced by the numerical simulations. After that, a series of parametric studies are performed to understand the influence of water saturation on the penetration performance of concrete. It is found that with the presence of pore water, penetration resistance of concrete increases with decreasing water saturation, indicating a higher projectile deceleration and lower penetration depth obtained in saturated targets. Numerical modelling and analysis will enhance our understanding of the vulnerability of concrete infrastructures subjected to near-field detonations or impacts.

1. Introduction

With the construction of large-scale buildings and structures, the local behaviour of mass concrete subjected to an extreme loading has become a prominent research topic for structural safety. Under near-field detonations or ballistic impacts, concrete suffers from high-intensity triaxial stress and high strain rates [1–6]. Moreover, as the surfaces of these concrete structures are often subjected to varying hydraulic conditions, a heterogeneous distribution of water saturation is usually created in concrete due to its relatively low permeability. Previous works [7–11] have exhibited that water saturation has a predominant influence on the response of concrete, especially at high-intensity stress levels. Therefore, the vulnerability of concrete infrastructures subjected to near-field detonations or impacts requires taking into account the influence of water saturation on concrete behaviour.

In the literature, a great number of static tests [7–9,11–19] have been conducted to study concrete behaviour under a wide range of confining pressures and water saturations. These experimental results have revealed the transition from brittle to ductile behaviour of concrete with the increase of confinement: irreversible deformation and pore collapse mechanism control the mechanical behaviour of concrete under high confining pressures. On the other hand, under dynamic loading, the influence of strain rate on the behaviour of concrete with different water saturations is only studied by several researchers [10,15,16,20–27]. Some researchers [8,16,17,23] have shown that wet concrete generally exhibits higher dynamic strength compared to dry one, indicating that wet concrete is more sensitive to strain rate than drier one. Nevertheless, contrasting findings have been reported in other experimental studied [10,25–27]. Dry or partially saturated concrete demonstrates better performance under dynamic loadings due to its greater ductility and ability to absorb more energy before failure. Conversely, more severe damage, fragmentation and reduced energy absorption capacity are observed in saturated concrete. The presence of water exacerbates spalling and fragmentation of concrete. To date, no general conclusion has been obtained on the influence of water saturation on the dynamic behaviour of concrete and further research

* Corresponding author.
E-mail address: hanbing.bian@polytech-lille.fr (H. Bian).

https://doi.org/10.1016/j.engstruct.2024.118563
Received 15 December 2022; Received in revised form 30 May 2024; Accepted 1 July 2024
Available online 14 July 2024

is still needed. However, in the aforementioned tests, due to large costs and technical challenges, the hydraulic response of concrete under dynamic loading conditions has not been clearly investigated.

In parallel, a series of micromechanics-based simulations [19,28–30] and macroscopic numerical studies [31–37] have been conducted to investigate the response of concrete at different levels of confining pressures and water saturation degrees. Recently, to take advantage and overcome shortcoming of micro/macro analysis, hybrid methods (for instance: FEM-SPH method [38] and FEM-DEM method [39]) are developed to study the dynamic behaviour of soil and rock materials. Until now, the application of such hybrid methods in the hydromechanical modelling of concrete under dynamic loading conditions is still very limited. For ease of use, the macroscopic method is then used in the present work. In the literature, only a few studies have been performed on the influence of water saturation on the penetration behaviour of concrete structures. Forquin et al. [40] and Bian et al. [35] have compared the penetration performance of dry and saturated concrete targets. They have revealed that dry target exhibited a higher penetration resistance than the wet one and explained this phenomenon by the influence of water saturation on the behaviour of concrete. After that, by adopting the pore water pressure as a function of volumetric strain, Zhao and Wen [41] and Huang et al. [42] have simulated the penetration of ballistic projectiles on concrete targets with three different water contents. Although the influence of water content on the mechanical behaviour of concrete is considered, hydraulic responses have not been analysed. Lately, Jia et al. [37] have studied the coupled hydromechanical behaviour of concrete under high confining pressures, but only under static loading conditions. As the microstructure of concrete includes a large quantity of capillary pores and cracks, water may be encased in this porous network and have a predominant influence on the response of concrete, especially at high stress levels. For instance, due to the short duration of intentional extreme loading and low permeability of concrete, a high interstitial pressure may be created in concrete structure during the penetration tunnel phase of impact and have a predominant influence on the response of concrete [3,20,43,44].

The present work focuses on the penetration performance of concrete target subjected to a rigid projectile, with special attention to the influence of water saturation. Not only the mechanical behaviour but also hydraulic responses (variation of fluid pressure with mass change and skeleton deformation) of concrete will be detailed here. A recent concrete model, proposed by Yang et al. [34], is improved to capture the penetration behaviour of concrete targets, including the effects of water saturation and strain rate. Four major modifications are made respectively to the relationship between porosity and volumetric dilatancy/compaction, the strain rate effects on material strength and pore collapse, the realization of full hydro-mechanical coupling under dynamic loading conditions and the analysis of coupled hydromechanical behaviour of concrete target under high strain rates. The poromechanics method is used to determine interstitial pressure related to skeleton deformation. In parallel, the impact of interstitial pressure on mechanical behaviour is taken into account using the Barcelona's concept. The performance of the modified model is firstly verified by simulating two dynamic compression tests at material level. After that, at the structure level, two penetration tests performed on saturated targets are analysed. The comparison of numerical results and experimental data shows that the proposed model is capable to predict, in a satisfactory manner, the penetration processes of a projectile into a concrete target. Finally, a series of numerical simulations are performed on concrete structures with different water saturations, and the influence of water saturation is then investigated.

2. Constitutive model for saturated and partially saturated concretes

In this study, the increment of total strain tensor $d\underline{\underline{\varepsilon}}$ is decomposed into an elastic part $d\underline{\underline{\varepsilon}}^e$ and a plastic part $d\underline{\underline{\varepsilon}}^p$:

$$d\underline{\underline{\varepsilon}} = d\underline{\underline{\varepsilon}}^e + d\underline{\underline{\varepsilon}}^p \tag{1}$$

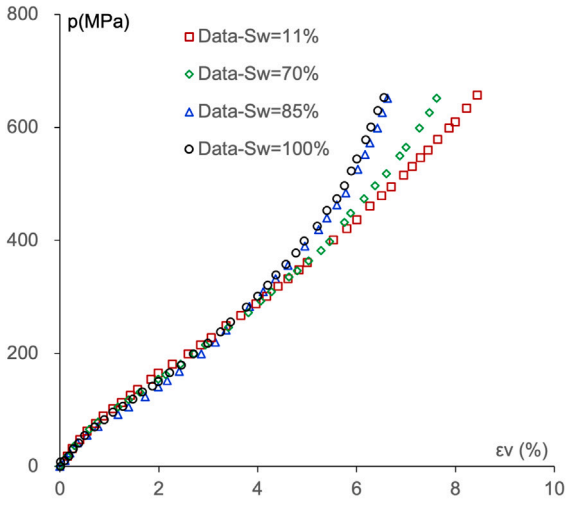

(a) Volumetric strain ε_v-mean stress p curves of hydrostatic compression tests

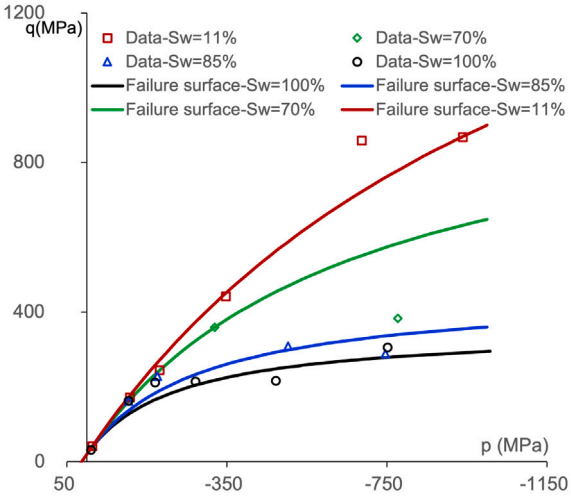

(b) Failure surface of triaxial compression tests

Fig. 1. Experimental results of laboratory tests with different water saturation degree S_w [8].

In the present work, the studied concrete is a standard concrete mixture, called R30A7 concrete, with a 28-days compressive strength of 30 MPa. Its composition is given in Vu et al. [8]. The studied material is assumed to be an isotropic porous medium saturated by a liquid water (noted by index w) and a gas mixture (noted by index g). The gas mixture is a perfect mixture of dry air (noted by index da) and vapour (noted by index va). Denoting the pressure of the fluid phase $\alpha(w, va, da)$, the pressure of gas mixture p_g is expressed by the following relation:

$$dp_g = dp_{va} + dp_{da} \tag{2}$$

The capillary pressure p_{cp} is defined as follow:

$$dp_{cp} = dp_g - dp_w \tag{3}$$

Based on previous works [45,46], the effects of liquid and gas pressure are characterized by an equivalent pore pressure π:

$$d\pi = dp_g - S_w\left(p_{cp}\right) dp_{cp}; \quad \pi = \int d\pi \tag{4}$$

S_w denotes water saturation degree. With the assumption that S_w depends only on the capillary pressure p_{cp} under isothermal condition and the adoption of the previous equivalent pore pressure (Eq. (4)), the elastic constitutive relations are expressed as:

$$d\underline{\underline{\sigma}} = \left(K_b - \frac{2}{3}G\right) d\varepsilon_v^e \underline{\underline{\delta}} + 2G d\underline{\underline{\varepsilon}}^e - b d\pi \underline{\underline{\delta}} \tag{5}$$

In practice, as the variation of gas pressure is much smaller than that of water pressure in the penetration test, we adopt $dp_g = 0$ in the present work and then we have $p_{cp} = -p_w$. When the porous material is subjected to macroscopic stress $\underline{\underline{\sigma}}$ and internal pressure p_w, the poroelastic constitutive equations of unsaturated porous media can be rewritten as follows: [46,47].

$$\begin{cases} d\underline{\underline{\sigma}} = \left(K_b - \frac{2}{3}G\right) d\varepsilon_v^e \underline{\underline{\delta}} + 2G d\underline{\underline{\varepsilon}}^e - bS_w dp_w \underline{\underline{\delta}} \\ dp_w = M_{ww}\left[\frac{dm_w}{\rho_w} - bS_w d\varepsilon_v^e\right] \end{cases} \tag{6}$$

K_b and G are respectively drained bulk modulus and shear modulus of the porous medium. ε_v^e represents the elastic volumetric strain. $\underline{\underline{\delta}}$ denotes the second-order unit tensor. The Biot's modulus M_{ww} can be identified as follows:

$$\frac{1}{M_{ww}} = \phi \frac{\partial S_w}{\partial p_w} + \frac{\phi S_w}{K_w} + N S_w^2, \quad N = \frac{(1-b)(b-\phi)}{K_b} = \frac{(b-\phi)}{K_s} \tag{7}$$

b is the Biot's coefficient of porous medium and ϕ represents the porosity. K_s and K_w denote the bulk modulus of solid matrix and the compressibility modulus of liquid water, respectively. In unsaturated case, water pressure is related to water saturation by the water retention curve:

$$S_w = \left[\frac{1}{1.0 + (-p_w/a_w)^{b_w}}\right]^{(1-\frac{1}{b_w})}, a_w = 2.0E6, b_w = 1.54 \tag{8}$$

In practice, the penetration of projectile lasts only a few microseconds and there is insufficient time for pore water to escape from the sample. Therefore, undrained condition could be adopted in the numerical analysis of coupled hydro-mechanical behaviour of concrete subjected to a rigid projectile. Under undrained condition ($m_w = 0$), the evolution of water pressure can be obtained by using the Eq. (6):

$$dp_w = -bS_w M_{ww} d\varepsilon_v^e \tag{9}$$

2.1. An enhanced plastic model for concrete under high confining pressures

When a concrete is subjected to ballistic impacts, the involved mechanisms are complex: compressive damage (cratering) on the frontal surface, irreversible deformation and pore collapse around the penetration tunnel, and eventual tensile damage (scabbing) on the opposite side. The basic mechanical behaviour of concrete is elastoplastic coupled with damage. However, the present work focuses specifically on the influence of water saturation on the penetration performance of concrete targets subjected to a rigid projectile. At high stress levels obtained in concrete during the penetration of rigid impact, two crucial mechanisms come into play: irreversible deformation and pore collapse. In order to capture the most significant influence of interstitial pressure on concrete responses, denoting the highest interstitial pressure level, the damage mechanism inducing pressure decrease is deliberately neglected in the present work.

In practical applications, concrete structures typically experience static or quasi-static loadings throughout their service life, occasionally encountering unexpected dynamic impacts. As previously noted, while numerous experimental studies have indicated the non-negligible influence of strain rate on concrete behaviour, it is still ongoing research without a conclusive consensus on the effect of strain rate on the mechanical behaviour of concrete. Therefore, the primary objective of the present study is to evaluate the possibility of employing a constitutive model, derived from static laboratory tests, for the numerical simulation of coupled hydro-mechanical phenomena involving dynamic tests. Moreover, since the present study represents a first series of numerical simulations to study the coupled hydro-mechanical behaviour of concrete target subjected to a rigid projectile penetration, for reasons of simplicity, a semi-empirical function [48] will be used to incorporate the influence of strain rate on pore collapse and material strength. Taking inspiration from the model proposed by Yang et al. [34], which successfully reproduces the static mechanical behaviour of concrete under a wide range of confining pressures, this constitutive model will be improved in the present work to describe the coupled hydro-mechanical behaviour of concrete under high-stress and high-strain-rate combined loading conditions.

Since the experimental studies have shown that water content plays an important role in concrete behaviour [8,9], the influence of water saturation on the mechanical behaviour of concrete should also be included in the plasticity formulation. In the literature, the influence of water saturation can be taken into account by using the Bishop's effective stress concept [46,49,50], or the net stress concept proposed by Alonso et al. [51], called Barcelona method. The main idea of the first approach is to extend the plastic functions of dry materials to saturated/partially saturated porous media by using a suitable effective stress. In the second type of approach, the concept of net stress (total mean stress plus gas pressure) is introduced into the plastic constitutive equations of unsaturated materials and the capillary pressure is used as a complementary force variable. As a result, plastic functions explicitly depend on the capillary pressure. As the Barcelona concept is fully based on experimental investigations and is widely used in the field of geomaterials, this approach is adopted in the present work. The plastic functions are expressed as functions of net stress $\underline{\underline{\sigma}}' = \underline{\underline{\sigma}} - \pi\underline{\underline{\delta}}$ and degree of water saturation S_w. Once concrete is saturated, $S_w = \overline{1}$, the equivalent pressure π is replaced by p_w. The net stress is then rewritten as : $\underline{\underline{\sigma}}' = \underline{\underline{\sigma}} - bp_w\underline{\underline{\delta}}$.

In the following section, two plastic mechanisms will be formulated respectively. The plastic strain increment is divided into two plastic parts: a shear plastic part $d\underline{\underline{\varepsilon}}^{ps}$ and a plastic pore collapse part $d\underline{\underline{\varepsilon}}^{pc}$:

$$d\underline{\underline{\varepsilon}}^{p} = d\underline{\underline{\varepsilon}}^{ps} + d\underline{\underline{\varepsilon}}^{pc} \tag{10}$$

As we know well that the porosity variation is essentially related to plastic strain increment, porosity variation $d\phi^p$ is also composed of two parts: $d\phi^{ps}$ related to shear plasticity and $d\phi^{pc}$ related to pore collapse plasticity.

$$d\phi^{p} = d\phi^{ps} + d\phi^{pc} \tag{11}$$

In the modelling of two plastic deformation mechanisms in geomaterials, the conventional approach combines two yield surfaces: a cap surface for plastic consolidation and a cone surface for plastic shearing [52–57]. As an alternative to avoid singularity points at the intersection of two surfaces, some plastic models with a single surface that combines the cap and cone have been proposed [58–60]. This framework, based on experimental investigation, can be applied in describing the fundamental mechanical behaviour of concrete. However, the primary objective of the present study is to offer a clear physical interpretation of two plastic mechanisms and propose the specific plastic functions, encompassing the distinct features observed in concrete behaviour. Concrete is conceptualized as a porous material, comprising an equivalent solid matrix and interconnected pores in the present work. The macroscopic behaviour of concrete is intricately shaped by the characteristics of both the solid matrix and the pores. The mechanical properties of the solid matrix are governed by three types of contact forces: capillary-related liquid contact forces, cemented solid contact forces, and frictional point contact forces. Plastic shearing and pore collapse manifest due to the gradual weakening of these contact forces. To model plastic shearing, we introduce a smooth quadratic yield function, offering an enhanced representation of the pronounced pressure sensitivity observed in concrete. This marks an improvement over the classic linear Mohr–Coulomb-type criteria [34].

For the pore collapse mechanism, we adopt Gurson's criterion [61,62], a micromechanics-based plastic yield criterion. This criterion explicitly links the plastic yield condition to the yield stress of the equivalent solid matrix and porosity [34].

2.1.1. Plastic pore collapse characterization

Inspired by the plastic model proposed by Gurson et al. [61] and Yang et al. [34], the following plastic yield function is expressed as the basic yield function of the pore collapse mechanism:

$$F_c\left(\underline{\underline{\sigma}}', \bar{\sigma}, S_w, \phi\right) = \frac{q^2}{\bar{\sigma}^2} + 2\phi\cosh\left(\frac{3p}{2\bar{\sigma}}\right) - 1 - \phi^2 = 0 \tag{12}$$

$$q = \sqrt{\frac{3}{2}\underline{\underline{s}}' : \underline{\underline{s}}'} \;; \quad \underline{\underline{s}}' = \underline{\underline{\sigma}}' - p\underline{\underline{\delta}} \;; \quad p = \frac{1}{3}tr\left(\underline{\underline{\sigma}}'\right) \tag{13}$$

where p is the mean net stress and q denotes the deviatoric net stress. ϕ represents the porosity of concrete. The coefficient $\bar{\sigma}$ represents the plastic yield stress of the concrete solid matrix, which depends on the mechanical properties of solid grains and on the various contact forces. Based on the experimental investigation from hydrostatic compression test, a plastic isotropic hardening law is proposed for the plastic pore collapse mechanism:

$$\bar{\sigma}\left(\dot{\varepsilon}, S_w\right) = \bar{\sigma}_{dyn}\left[1 + a\left(\varepsilon_M^{pc}\right)^n e^{\beta\varepsilon_M^{pc}}\right] \tag{14}$$

where ε_M^{pc} is the plastic volumetric strain due to the pore collapse process, $\varepsilon_M^{pc} = tr\left(\underline{\underline{\varepsilon}}^{pc}\right)$ taken as the internal hardening. $\bar{\sigma}_{dyn}$ denotes the initial yield stress of the solid matrix and a, n and β are three parameters of the hardening law. As indicated in experimental data (Fig. 1a), the stress–strain curves of hydrostatic compression tests depend strongly on the water saturation state. Moreover, the experimental results [16,20,21,63–65] have shown that the pore collapse process seems to be delayed under high strain rate conditions. By inducting a dynamic increase coefficient DIF, Xu et al. [42,48,66] have successfully study the influence of water content on the dynamic behaviour of concrete. With the assumption that S_w depends only on the capillary pressure under isothermal conditions (i.e., $S_w\left(p_{cp}\right)$), $\bar{\sigma}_{dyn}$ is defined as a function of the dynamic increase factor of compression $DIF^c_{S_w}$ and the yield stress of the solid skeleton under static loading conditions $\bar{\sigma}_0$:

$$\bar{\sigma}_{dyn} = DIF^c_{S_w}\cdot\bar{\sigma}_0(S_w) \;; \quad \text{with } \bar{\sigma}_0\left(S_w\right) = \bar{\sigma}_{0,d} - \left(\bar{\sigma}_{0,d} - \bar{\sigma}_{0,s}\right)e^{\left(-\xi_n\frac{1-S_w}{S_w}\right)} \tag{15}$$

$\bar{\sigma}_0$ denotes the initial yield stress of the solid matrix and can be identified from the transition point between the linear and non-linear parts of the volumetric strain-confining pressure curve of a static hydrostatic compression test. The function $\bar{\sigma}_0\left(S_w\right)$ should accordingly be a function of S_w, varying from the asymptotic value for saturated concrete, $\bar{\sigma}_{0,s}$, to that for dry concrete $\bar{\sigma}_{0,d}$. Based on the corrected strain-rate concept proposed by Kong et al. [66], the dynamic increase factor (DIF) of compression for wet concrete $DIF^c_{S_w}$ is defined as follows:

$$DIF^c_{S_w} = \left(DIF^t_{S_w} - 1\right)\frac{R^t_{S_w}}{R^c_{S_w}} + 1; DIF^t_{S_w} = \eta(\dot{\varepsilon}, S_w)\cdot DIF^t_0 \tag{16}$$

$R^t_{S_w}$ and $R^c_{S_w}$ represent the quasi-static tensile and compressive strengths, respectively, of concrete at different degrees of water saturation S_w. $DIF^t_{S_w}$ and DIF^t_0 denote the dynamic increase factors of tension for wet and dry concretes, respectively. To capture the effects of water saturation, $\eta(\dot{\varepsilon}, S_w)$ defines the ratio of $DIF^t_{S_w}$ and DIF^t_0 and is calculated by the following function [42]:

$$\eta(\dot{\varepsilon}, S_w) = \begin{cases} 1 & \text{if } \dot{\varepsilon} \le 10^{-5} \\ -\left(1 + 0.015S_w\right)^{-lg\dot{\varepsilon}-5} + 2 & \text{Otherwise} \end{cases} \tag{17}$$

The DIF for dry concrete DIF^t_0 is described by a semi-empirical formula proposed by Xu and Wen [48]:

$$DIF^t_0 = 5.5\left\{1 + 0.82\left[tanh\left(0.8\left(log\left(\frac{\dot{\varepsilon}}{\dot{\varepsilon_0}}\right) - 1.6\right)\right)\right]\right\} \tag{18}$$

$\dot{\varepsilon_0}$ is the reference strain rate $\dot{\varepsilon_0} = 1\ s^{-1}$.

According to the Eq. (12), the yield function of the pore collapse process depends also on the connected pores of concrete. By assuming that the plastic compressibility of solid grains may be neglected, the porosity change is expressed as following:

$$d\phi^{pc} = (1-\phi)\,tr\left(\underline{\underline{\varepsilon}}^{pc}\right) \tag{19}$$

To accurately describe the plastic volumetric deformation, a non-associated plastic flow rule is developed for the pore collapse process. By taking a similar form as the yield function, the following function is used as the plastic potential:

$$Q_c\left(\underline{\underline{\sigma}}', \bar{\sigma}, \phi\right) = \frac{q^2}{\bar{\sigma}^2} + 2\phi\cosh\left(\frac{3p}{2\bar{\sigma}}\right) \tag{20}$$

2.1.2. Plastic shear characterization

Based on the experimental data obtained under various loading paths, a curved yield surface is necessary to take into account the strong pressure dependence. Based on the research work of Yang at al. [34], the following yield function is employed:

$$F_s(\underline{\underline{\sigma}}', \gamma^{ps}, S_w) = q + \alpha_s(p - c_3)\frac{c_1}{\left(1 - c_{2,dyn}\frac{p}{p_r}\right)} = 0 \tag{21}$$

p_r is a reference pressure, one takes $p_r = 1$ MPa. The parameter c_1 is an equivalent friction coefficient, c_3 denotes the cohesion coefficient of material and c_2 represents the nonlinearity of yield surface. Moreover, as the experimental investigation exhibits that the curvature of the deviatoric yield surface is dependent on water saturation and strain rate, this dependency is here interpreted by the fact that the parameter $c_{2,dyn}$ is expressed as a function of S_w and strain rate $\dot{\varepsilon}$. Inspired by the formulation of $\bar{\sigma}_{dyn}$ presented in the previous section, for the reason of simplicity, the parameter $c_{2,dyn}$ is defined as a function of $DIF^c_{S_w}$ and the yield stress under static loading conditions $c_2(S_w)$:

$$c_{2,dyn} = DIF^c_{S_w}\cdot c_2(S_w) \;; \quad \text{with } c_2(S_w) = c_{2d} - (c_{2d} - c_{2s})e^{\left(-\xi_{c_2}\frac{1-S_w}{S_w}\right)} \tag{22}$$

$c_2(S_w)$ describes the dependence of parameter c_2 on the degree of water saturation S_w. The parameter ξ_{c2} controls the evolution of c_2 with S_w, while c_{2s} and c_{2d} are respectively the values of c_2 in fully saturated and dry concretes.

The plastic hardening law α_s is proposed as follows:

$$\alpha_s = 1.0 - \left(1.0 - \alpha_s^0\right)e^{-\zeta\gamma^{ps}} \tag{23}$$

$$\gamma^{ps} = \int\sqrt{\frac{2}{3}d\underline{\underline{e}}^{ps}d\underline{\underline{e}}^{ps}}/\chi_p; d\underline{\underline{e}}^{ps} = d\underline{\underline{\varepsilon}}^{ps} - \frac{d\varepsilon^{ps}_{kk}}{3}\underline{\underline{\delta}}; \chi_p = \frac{\left\langle p' - \frac{q}{3} - p_r\right\rangle}{p_r} \tag{24}$$

the parameter ζ controls the rate of plastic hardening.

In order to describe the volumetric transition from contractancy to dilatancy observed in triaxial compression tests, a non-associated plastic flow rule must be defined:

$$Q_s(\underline{\underline{\sigma}}', \gamma^{ps}, S_w) = q + \eta I ln(I/I_0) = 0, I = p - c_3 \tag{25}$$

the parameter I_0 defines the intersection of the plastic potential surface with the p axis. the parameter η defines the slope of the boundary between contractive and dilatant zones.

Inspired by the Eq. (19), the porosity change related to shear plasticity is expressed as following:

$$d\phi^{ps} = (1-\phi)\,tr\left(\underline{\underline{\varepsilon}}^{ps}\right) \tag{26}$$

In triaxial compression tests [8], one observes that once the confining pressure is greater than the pore collapse yield stress of the material $\bar{\sigma}$, the volumetric compaction is dominant and the volumetric dilatancy may be only observed just before the sample failure. Assuring that the volumetric compaction observed under high confining pressures is only

related to the pore closure, the plastic part of porosity variation $d\phi^p$ is determined as follows:

$$d\phi^p = \begin{cases} \langle d\phi^{ps}\rangle + d\phi^{pc} & \text{if } p \geq \bar{\sigma} \\ d\phi^{ps} & else \end{cases} \tag{27}$$

The bracket $\langle d\phi^{ps}\rangle$ means that only the positive value will be taken into consideration: $\langle d\phi^{ps}\rangle = 0$ if $\langle d\phi^{ps}\rangle \leq 0$ and $\langle d\phi^{ps}\rangle = d\phi^{ps}$ if $d\phi^{ps} > 0$.

2.2. Coupling and numerical implementation of two plastic mechanisms in saturated and partially saturated concretes

For the loading history where only the pore collapse mechanism is activated (for instance, in the hydrostatic compression tests), the plastic flow is written as:

$$d\underline{\underline{\varepsilon}}^{pc} = d\lambda_c \frac{\partial Q_c}{\partial \underline{\underline{\sigma}}'} \tag{28}$$

$$\frac{\partial Q_c}{\partial \underline{\underline{\sigma}}'} = \frac{\partial Q_c}{\partial q}\frac{\partial q}{\partial \underline{\underline{\sigma}}'} + \frac{\partial Q_c}{\partial p}\frac{\partial p}{\partial \underline{\underline{\sigma}}'} = \frac{3\underline{\underline{s}}'}{\bar{\sigma}^2} + \frac{\phi}{\bar{\sigma}}\sinh\left(q_1\frac{3p}{2\bar{\sigma}}\right)\underline{\underline{\delta}} \tag{29}$$

The plastic multiplier $d\lambda_c$ can be determined by the plastic consistency condition:

$$d\lambda_c = \frac{\frac{\partial F_c}{\partial \underline{\underline{\sigma}}'} : \underline{\underline{\underline{\underline{C}}}} : d\underline{\underline{\varepsilon}} + \frac{\partial F_c}{\partial \bar{\sigma}}\frac{\partial \bar{\sigma}}{\partial S_w}\frac{\partial S_w}{\partial p_{cp}}dp_{cp}}{\frac{\partial F_c}{\partial \underline{\underline{\sigma}}'} : \underline{\underline{\underline{\underline{C}}}} : \frac{\partial Q_c}{\partial \underline{\underline{\sigma}}'} - \frac{\partial F_c}{\partial \bar{\sigma}}\frac{\partial \bar{\sigma}}{\partial tr\left(\underline{\underline{\varepsilon}}^{pc}\right)}\frac{\partial Q_c}{\partial p} - \frac{\partial F_c}{\partial \underline{\underline{\sigma}}'}\phi(1-\phi)\frac{\partial Q_c}{\partial p}} \tag{30}$$

For the loading history where only the plastic shear mechanism is developed in concrete, the plastic flow rule is written as following:

$$d\underline{\underline{\varepsilon}}^{ps} = d\lambda_s \frac{\partial Q_s}{\partial \underline{\underline{\sigma}}'} \tag{31}$$

$$\frac{\partial Q_s}{\partial \underline{\underline{\sigma}}'} = \frac{\partial Q_s}{\partial q}\frac{\partial q}{\partial \underline{\underline{\sigma}}'} + \frac{\partial Q_s}{\partial p}\frac{\partial p}{\partial \underline{\underline{\sigma}}'} = \frac{3}{2}\frac{\underline{\underline{s}}}{q} + \frac{1}{3}\eta[1+(\frac{I}{I_0})]\underline{\underline{\delta}} \tag{32}$$

The plastic multiplier can be determined by the plastic consistency condition:

$$d\lambda_s = \frac{\frac{\partial F_s}{\partial \underline{\underline{\sigma}}'} : \underline{\underline{\underline{\underline{C}}}} : \underline{\underline{\varepsilon}} + \frac{\partial F_s}{\partial c_2}\frac{\partial c_2}{\partial S_w}\frac{\partial S_w}{\partial p_c p}dp_c p}{\frac{\partial F_s}{\partial \underline{\underline{\sigma}}'} : \underline{\underline{\underline{\underline{C}}}} : \frac{\partial Q_s}{\partial \underline{\underline{\sigma}}'} - \frac{\partial F_s}{\partial \alpha_s}\frac{\partial \alpha_s}{\partial \gamma^{ps}}\sqrt{\frac{2}{3}(\underline{\underline{\underline{\underline{K}}}} : \frac{\partial Q_s}{\partial \underline{\underline{\sigma}}'}) : (\underline{\underline{\underline{\underline{K}}}} : \frac{\partial Q_s}{\partial \underline{\underline{\sigma}}'})}} \tag{33}$$

In a general loading history case, two plastic deformation mechanisms can be activated simultaneously. A non-linear system of consistency conditions should be solved to determine the increments of plastic deformation:

$$\begin{cases} df_c = \frac{\partial f_c}{\partial \underline{\underline{\sigma}}'}d\underline{\underline{\sigma}}' + \frac{\partial f_c}{\partial \phi}d\phi + \frac{\partial f_c}{\partial \bar{\sigma}}d\bar{\sigma} = 0 \\ df_s = \frac{\partial f_s}{\partial \underline{\underline{\sigma}}'}d\underline{\underline{\sigma}}' + \frac{\partial f_s}{\partial \alpha_s}\frac{\partial \alpha_s}{\partial \gamma^{ps}}d\gamma^{ps} = 0 \end{cases} \tag{34}$$

By introducing the state equations and the hardening laws in the above equations, we obtain the system of equations to determine two plastic multipliers:

$$\begin{vmatrix} \frac{\partial F_c}{\partial \underline{\underline{\sigma}}'} : \underline{\underline{\underline{\underline{C}}}} : \frac{\partial Q_c}{\partial \underline{\underline{\sigma}}'} - H_{cc} & \frac{\partial F_c}{\partial \underline{\underline{\sigma}}'} : \underline{\underline{\underline{\underline{C}}}} : \frac{\partial Q_s}{\partial \underline{\underline{\sigma}}'} - H_{cs} \\ \frac{\partial F_s}{\partial \underline{\underline{\sigma}}'} : \underline{\underline{\underline{\underline{C}}}} : \frac{\partial Q_c}{\partial \underline{\underline{\sigma}}'} - H_{sc} & \frac{\partial F_s}{\partial \underline{\underline{\sigma}}'} : \underline{\underline{\underline{\underline{C}}}} : \frac{\partial Q_s}{\partial \underline{\underline{\sigma}}'} - H_{ss} \end{vmatrix} \begin{vmatrix} d\lambda_c \\ d\lambda_s \end{vmatrix} = \begin{vmatrix} R_c \\ R_s \end{vmatrix}$$

$$\text{with } \begin{cases} R_c = \frac{\partial f_c}{\partial \underline{\underline{\sigma}}'} : \underline{\underline{\underline{\underline{C}}}} : d\underline{\underline{\varepsilon}} + \frac{\partial f_c}{\partial S_w}\frac{\partial S_w}{\partial p_{cp}}dp_{cp} \\ R_s = \frac{\partial f_s}{\partial \underline{\underline{\sigma}}'} : \underline{\underline{\underline{\underline{C}}}} : d\underline{\underline{\varepsilon}} + \frac{\partial f_s}{\partial S_w}\frac{\partial S_w}{\partial p_{cp}}dp_{cp} \\ H_{cc} = \frac{\partial F_c}{\partial \phi}(1-\phi)\text{tr}(\frac{\partial Q_c}{\partial \underline{\underline{\sigma}}'}) + \frac{\partial F_c}{\partial \bar{\sigma}}\frac{\partial \bar{\sigma}}{\partial \epsilon_M^c}\frac{\partial Q_c}{\partial \underline{\underline{\sigma}}'} \\ H_{ss} = \frac{\partial F_s}{\partial \alpha_s}\frac{\partial \alpha_s}{\partial \gamma^{ps}}\sqrt{\frac{2}{3}(\underline{\underline{\underline{\underline{K}}}} : \frac{\partial Q_s}{\partial \underline{\underline{\sigma}}'}) : (\underline{\underline{\underline{\underline{K}}}} : \frac{\partial Q_s}{\partial \underline{\underline{\sigma}}'})} \end{cases} \tag{35}$$

In these relations, the fourth order tensor $\underline{\underline{\underline{\underline{C}}}}$ is the elastic stiffness tensor of porous media, which is written in the following form:

$$\underline{\underline{\underline{\underline{C}}}} = 2G\underline{\underline{\underline{\underline{K}}}} + 3K\underline{\underline{\underline{\underline{J}}}} \tag{36}$$

Isotropic symmetric fourth order tensors $\underline{\underline{\underline{\underline{K}}}}$ and $\underline{\underline{\underline{\underline{J}}}}$ are defined by:

$$\underline{\underline{\underline{\underline{J}}}} = \frac{1}{3}\left(\underline{\underline{\delta}}\otimes\underline{\underline{\delta}}\right); \underline{\underline{\underline{\underline{K}}}} = \underline{\underline{\underline{\underline{I}}}} - \underline{\underline{\underline{\underline{J}}}}; I_{ijkl} = \frac{1}{2}\left(\delta_{ik}\delta_{jl} + \delta_{il}\delta_{jk}\right) \tag{37}$$

$\underline{\underline{\underline{\underline{I}}}}$ is the symmetric fourth order unit tensor. The coefficients H_{cs} and H_{sc} represent the coupling between the two plastic processes through the related plastic hardening laws. In order to improve the computational efficiency, a weak coupling between plastic processes through the related plastic hardening laws is supposed by adopting $H_{cs} = H_{sc} = 0$.

By using the previous general formulation, the proposed model is able to describe the hardening interaction between the two plastic mechanisms and the interstitial pressure. It is then implemented in the finite element code Abaqus/Explicit, using a dynamic user-defined material (VUMAT) model. This integration process is executed at each Gauss point of the elements. At the beginning of each step, an increment of total strain is applied to the Gauss point. After that, the corresponding increments of stress, interstitial pressure and plastic strains are estimated using the constitutive equations and loading-unloading conditions. The solution schema for the k^{th} step is elaborated in Fig. 2.

3. Calibration of the enhanced model and numerical validation

In this section, the model's parameters are firstly calibrated by using a series of hydrostatic and triaxial compression tests performed under different confining pressures and water saturation states. After that, two dynamic tests are simulated to demonstrate the potential application of the enhanced model, derived from the static laboratory tests, in the numerical analysis of coupled hydro-mechanical behaviour of concrete under high strain rates with different water contents. We begin with the parameter calibration.

3.1. Parameter calibration

The proposed model consists of 11 parameters: two elastic parameters (E, ν), four parameters $(\bar{\sigma}_0, a, \beta, n)$ related to pore collapse plasticity and five parameters for shear plasticity $(c_1, c_2, c_3, \zeta, \eta)$.

Both elastic parameters can be determined from the linear part of stress–strain curves before the initiation of damage and plastic deformation. Concerning the parameters of pore collapse plasticity, they can be identified by using the experimental results of hydrostatic compression tests. The initial pore collapse stress $\bar{\sigma}_0$ is obtained from the transition point from linear to non-linear part of stress–strain curve in a hydrostatic compression test (Fig. 1). The three hardening parameters (a, β, n) can be identified from hydrostatic compression test by drawing plastic volumetric strain versus mean stress. By using the values of $\bar{\sigma}_0$ obtained in the samples with different S_w, the parameter ξ_{σ_0}, controlling the evolution $\sigma_0 n$ in function of S_w (Eq. (14)), can be identified. The characteristic values of these parameters are given as follows: $\bar{\sigma}_{0,d} = 70$ MPa, $\bar{\sigma}_{0,s} = 35$ MPa, $a = 150$, $n = 1.25$, $\beta = 70$, $\xi_{\sigma_0} = 0, 2$.

The three parameters of shear failure surface (c_1, c_2, c_3) can be identified by plotting the peak stresses obtained in triaxial compression tests with different confining pressures in the $p-q$ plane (Fig. 1). The hardening parameter ζ can be obtained by drawing the hardening function versus the plastic distortion α_s-γ^{ps} (Eq. (23)). Finally, the parameter η is obtained by plotting the volumetric compressibility/dilatancy transition points in the $p-q$ plane. After that, by using the

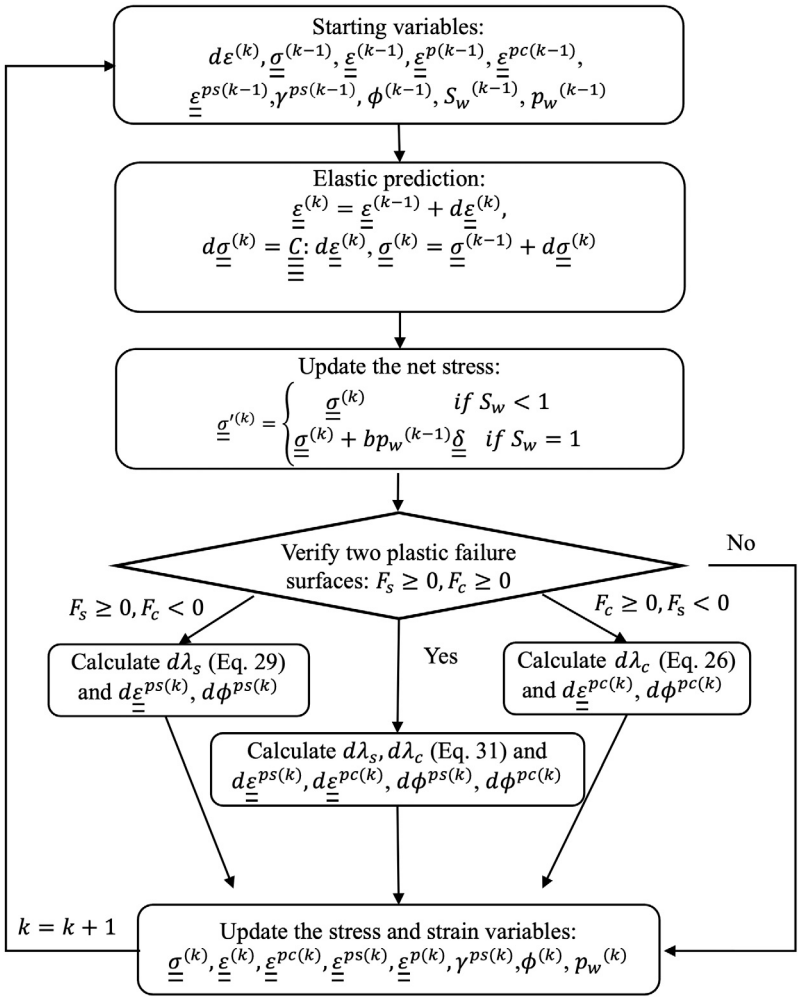

Fig. 2. Flow chart for numerical implementation of the improved plastic model at the kth step.

value of c_2 identified on the samples with different S_w, the parameter ξ_{c2}, controlling the evolution c_2 in function of S_w (Eq. (22)), can be identified. Finally, one has $c_1 = 1.8$ and $c_3 = 12.3$ MPa, $\zeta = 500$, $\eta = 1.55$, $c_{2s} = 0.0085$, $c_{2d} = 0.002$, $\xi_{c2} = 0.3$.

3.2. Dynamic oedometric compression tests

The performance of the proposed model under static loading conditions has been verified by Jia et al. [37], via the simulation of a series of hydrostatic compression tests and oedometric compression tests. The good agreement between the numerical simulations and experimental data allows us to confirm that the constitutive model is capable of describing concrete responses under a wide range of confining pressures and water saturation states. Since the present study focuses on the coupled hydromechanical behaviour of a concrete target subjected to a rigid projectile, the adopted constitutive model and numerical method will be verified at the material point level by simulating two dynamic compression tests performed on saturated and dry concretes.

In the oedometric compression test, as the sample is tightly enclosed in a confinement vessel and compressed by an axial stress, the responses of concrete can be studied at different levels of confining pressure. These two dynamic tests have been performed with the help of a large Split Hopkinson Pressure Bar facility, called SHPB system. The average strain rates were about the order of 10^2/s. Moreover, since the sample set-up inside the cell prevented the water loss, undrained conditions were guaranteed during the laboratory tests. The detail of the experimental set-up can be found in Piotrowska and Forquin [16]. In the numerical simulation, the axial displacements are blocked on all the lateral surfaces and the bottom of the sample while the external force is only applied on its upper surface. Moreover, an impermeable conditions is applied on all the external boards of the sample.

The numerical results of the saturated concrete sample are firstly analysed (Fig. 3a). Three phases are identified in the mean stress p - deviatoric stress q curve. At the beginning, an elastic phase is observed. When the applied stress is greater than the plastic yield stress of pore collapse plasticity $\bar{\sigma}$, a plastic hardening phase is clearly observed due to pore collapse. Once the pores cannot be continuously compacted, the deviatroic stress tends to converge to a constant value. This phenomenon is related to the fact that under high confining pressures, concrete loses its cohesion and behaves like a saturated granular material. The pore pressure rises and dominates the applied stress. One can observe that pore water has a significant impact on the mechanical behaviour of concrete.

After that, the dynamic test of dry concrete is simulated. In the mean stress-deviatoric stress ($p - q$) curve (Fig. 3b), a more distinct elastic phase is observed in the experimental results compared to the saturated sample. Consequently, with the occurrence of pore collapse, the deviatoric stress gradually increases as the mean stress increases. However, the finale stabilization of deviatoric stress is not observed in dry concrete due to the absence of pore water. If the applied stress continues to increase, the behaviour of dry concrete will approaches that of the saturated sample, resulting from the pores closure. In general, a good agreement is obtained between the numerical simulation

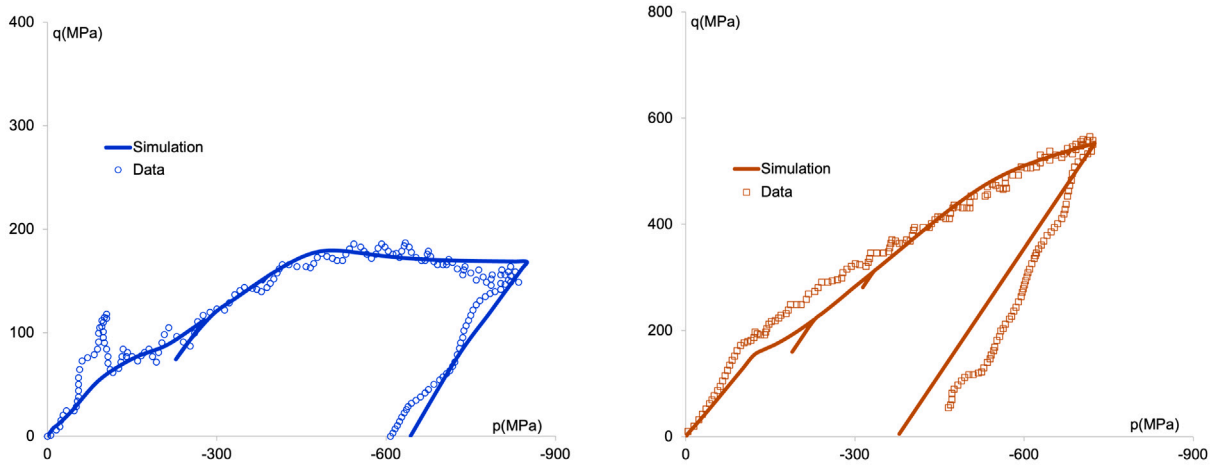

Fig. 3. Simulation of mean stress p - deviatoric stress q curves of two one-dimensional dynamic compression tests performed on saturated (a) and dry (b) concretes.

and experiment data, including the stress limit of pore collapse and the peak values observed in the laboratory tests.

Based on the obtained results, one can conclude that the adopted constitutive model and numerical method are capable of reproducing satisfactorily and quantitatively the responses of saturated and dry concretes under dynamic loading conditions. After that, the penetration tests performed on concrete targets with different S_w will be simulated and studied in the next section.

4. Numerical simulation of the penetration tests performed on concrete targets

The penetration tests performed with two different initial velocities of projectile (V_p = 227 and 347 m/s) will be studied here. In the penetration test, an ogive-nose projectile with weight of 2.4 kg (Nose radius to diameter ratio = 5.77 with a diameter of R = 52 mm) was used to hit the centre of the cylindrical unreinforced concrete target (with a diameter of 80 cm and a thickness of 80 cm), confined in a steel sleeve of 15 mm in thickness. An acceleration recorder system was also installed in the steel projectile to register the track of its axial deceleration. The detail of laboratory tests can be found in Bian et al. [47]. In the numerical simulations, the hard projectile is represented as a rigid body while the initial velocity is applied on its centre. The steel ring, confining the concrete target, is simulated by a von Mises elastoplastic model with a yield stress of order 500 MPa. As the concrete target is prepared and preserved in saturated limewater until the realization of penetration test, the concrete target can be considered as fully saturated during the penetration test.

4.1. Preliminary numerical study

To adopt a reasonable numerical model, some preliminary calculations have been performed, including the influence of mesh size, 2D/3D configuration, erosion criterion and friction condition on the interface between projectile and concrete target.

Firstly, the influence of mesh type/size is studied. By using the same mesh size, two numerical calculations have been performed in 3D and 2D axisymmetric conditions, respectively. In the 3D numerical model, the total cylindrical concrete target and projectile are taken into account while only one half of them are used in the 2D axisymmetric model. As the projectile is considered as rigid and used to hit the centre of the isotope concrete target, almost the same results are obtained 3D and 2D configurations. Therefore, 2D axisymmetric configuration and an uniform mesh composed of quadrilateral elements are adopted in the present work (Fig. 4) to reduce computational costs. Moreover, in order to get reliable results with a suitable mesh size, three 2D calculations with different mesh sizes (80 000, 150 000 and 240 000 quadrilateral elements) have been performed and a negligible difference is observed among them. Therefore, in the present work, the cylindrical concrete target is divided in 200 elements in the radial direction and 400 elements in the depth direction, i.e., 80 000 quadrilateral elements (see Fig. 4).

When concrete structures are subjected to a rigid projectile, the failure of concrete inevitably involves in large strain, resulting in mesh entanglement and distortion. As a result, the numerical analysis will be prematurely terminated. To address this, an element erosion technique must be carefully implemented. Under compression loading, an equivalent strain-based erosion criterion or a damage-based criterion is generally adopted [40–42,67–70]. The primary focus of the present study is to investigate the coupled hydro-mechanical behaviour of concrete targets subjected to a rigid projectile. Special attention is paid on the effects of pore water pressure, while damage is neglected to minimize its effect on the pressure evolution. Accordingly, a strain-based criterion is then adopted in the present work. Common strain-based erosion criteria include the incremental plastic strain [42], instantaneous geometric strain [69], and maximum shear strain [70], each with specific formulations and applications in studying the behaviour of concrete structures subjected to impact loads. Inspired by previous research, in the present work, a equivalent plastic strain criterion is adopted to reproduce the shear failure of concrete generally observed under compression loading and take into account the influence of confining pressure. When the elements, in which the equivalent plastic deformation γ^p reaches a predefined value $\gamma^p_{\max}$, will be then eliminated. To study the influence of $\gamma^p_{\max}$, three numerical simulations with different values of $\gamma^p_{\max}$ ($\gamma^p_{\max}$ = 0.5, 1 and 2) have been performed. Finally, the critical value of $\gamma^p_{\max}$ = 2 is adopted for the best fitting of the experimental results of the penetration test (see Fig. 5).

Moreover, the penetration of projectile into the concrete target induces a friction force at the interface between the concrete target and projectile. However, this friction force is very difficult to identify experimentally. In view of this, the influence of this phenomenon is also analysed by using three values of the friction coefficient. One observes that the friction coefficient has an important impact on the penetration behaviour of projectile: the amplitude of the projectile deceleration increases with increasing friction coefficient f. Its value is also determined by the best fitting of the experimental results: f = 0.2 (see Fig. 6).

Based on the preliminary results, the friction coefficient f = 0.2, the erosion criterion $\gamma^p_{\max}$ = 2 and a 2D asymmetric numerical model

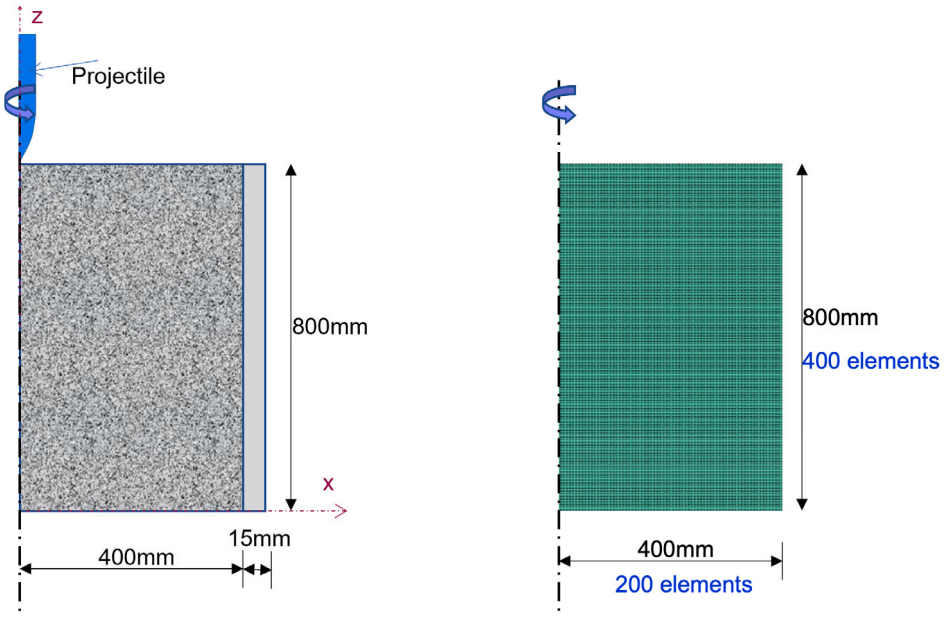

(a) Concrete target and steel ring (b) Used mesh for concrete target

Fig. 4. Geometry and used mesh for the penetration tests.

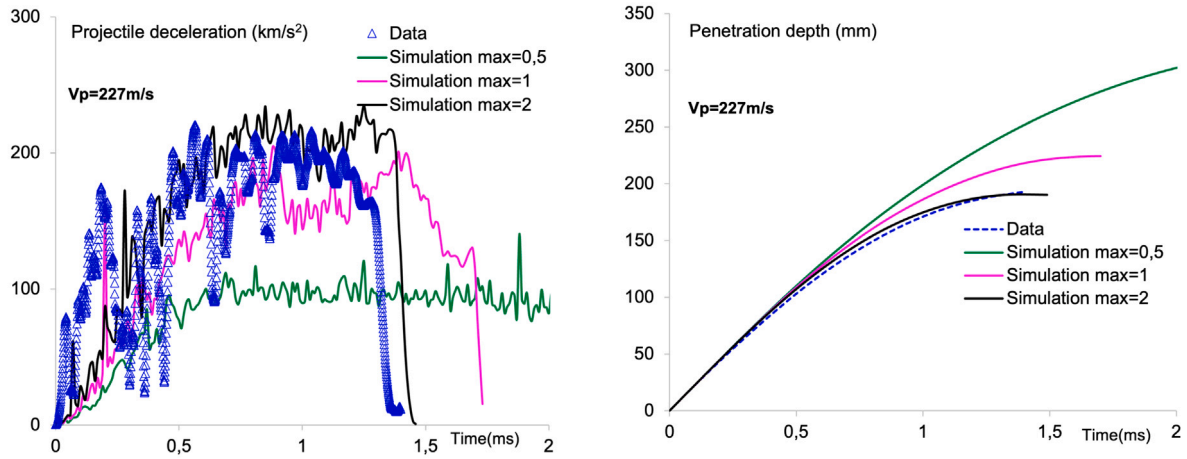

(a) Projectile deceleration (b) Penetration depth

Fig. 5. Influence of maximum equivalent plastic γ^{p}_{max} on the numerical results of penetration test with the projectile velocity $V_p = 227$ m/s.

are adopted in the present work to simulate the penetration tests. All the calculations are synthesized in Table 1 (see Fig. 6).

4.2. Projectile penetration tests performed on saturated concrete targets

Two penetration tests performed on saturated concrete will be simulated by using the improved constitutive model. The numerical results of penetration depth, projectile deceleration and projectile velocity are simulated and analysed in this section.

The projectile deceleration curves of the penetration tests with two V_p are firstly given in Fig. 7. Three successive phases are generally observed : projectile penetration, tunnelling and rapid stop. In the projectile penetration phase, a strong increase of projectile deceleration is observed. After that, the deceleration rate tends to stabilize during the tunnelling phase and exhibits a sharp stop of the projectile at the end of test. The basic behaviour of the projectile is satisfactorily simulated by the numerical results. By comparing the results of two different initial velocities, one observes that the amplitude of projectile deceleration increases with increasing projectile velocity. This observation is accurately captured by the numerical simulations, with the consideration of the effects of strain rate.

The evolutions of penetration depth in two tests are presented in Fig. 8. One observes that the penetration depth increases progressively with time. For two tests with different V_p, a very good concordance is generally obtained between the numerical simulations and experimental data. The comparison of two tests exhibits that the penetration depth increases with increasing projectile velocity : the penetration depth is equal to 190 mm in the test with V_p = 227 m/s while the projectile of V_p = 347 m/s penetrates in the concrete target with a depth of 284 mm. As a result, we can conclude that the influence of projectile velocity on the penetration depth of projectile is also captured by the numerical simulation. According to the projectile velocity (Fig. 9), it is observed that the projectile velocity decreases progressively with the penetration of projectile into the target. In general, a good concordance is observed

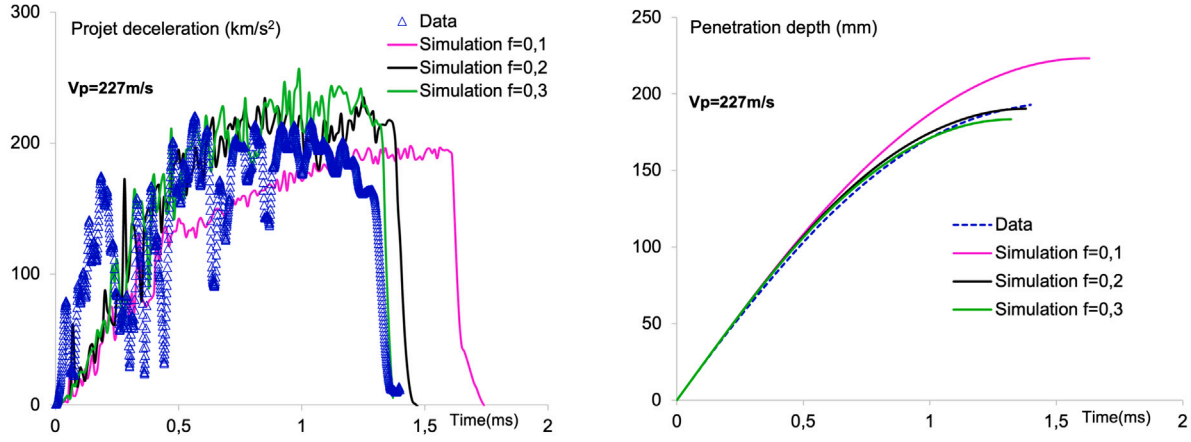

(a) Projectile deceleration (b) Penetration depth

Fig. 6. Influence of the friction coefficient f on the numerical results of penetration test with the projectile velocity $V_p = 227$ m/s.

Table 1
Numerical simulations of penetration tests with different water saturation degree S_w.

Case	N°	S_w (%)	p_w	$\gamma^p_{\max}$	Strain rate	V_p (m/s)	Numerical results	
							Projectile deceleration mean value (m/s²)	Penetration depth (mm)
Saturated	D1	100	Yes	2	$DIF^c_{S_w}$	227	158	190
	D2					347	243	282
	S1					227	174	180
	S2					347	218	307
	1			3	$DIF^c_{S_w} = 1$	227	163	190
	2					347	197	327
Numerically dry	3	0	No			227	185	170
	4					347	240	281
Dry	5					227	216	138
	6					347	303	226
Partially saturated	7	60	Yes			227	182	168
	8					347	275	266
	9	80				227	173	175
	10					347	257	283

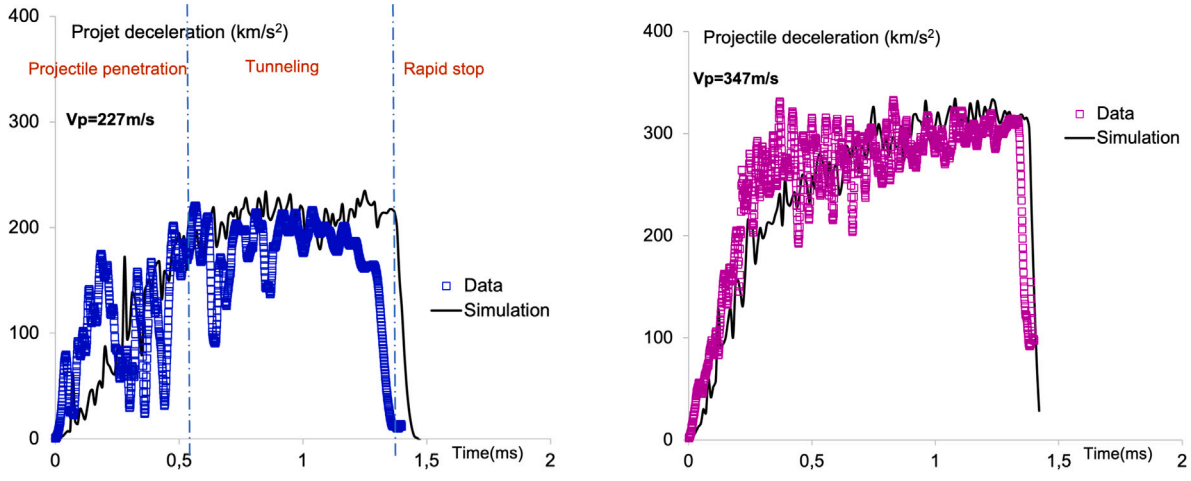

(a) $V_p = 227$ m/s (b) $V_p = 347$ m/s

Fig. 7. Projectile deceleration versus time in the penetration tests of saturated concrete targets.

between the experimental data and numerical results. Again, the effects of projectile velocity are well captured by the numerical results.

Finally, the distributions of interstitial pressure in the concrete targets with two V_p are discussed. The numerical results of the penetration test with V_p = 227 m/s are firstly given at six different moments (Fig. 10). An important overpressure is observed around the tunnel field of projectile trajectory and this overpressure zone progresses forward in the target during the projectile penetration process. The maximum value of overpressure (p_w^{max}) initially increases with the projectile penetration (p_w^{max} = 117 MPa at t = 0.2 ms), then tends to stabilize towards

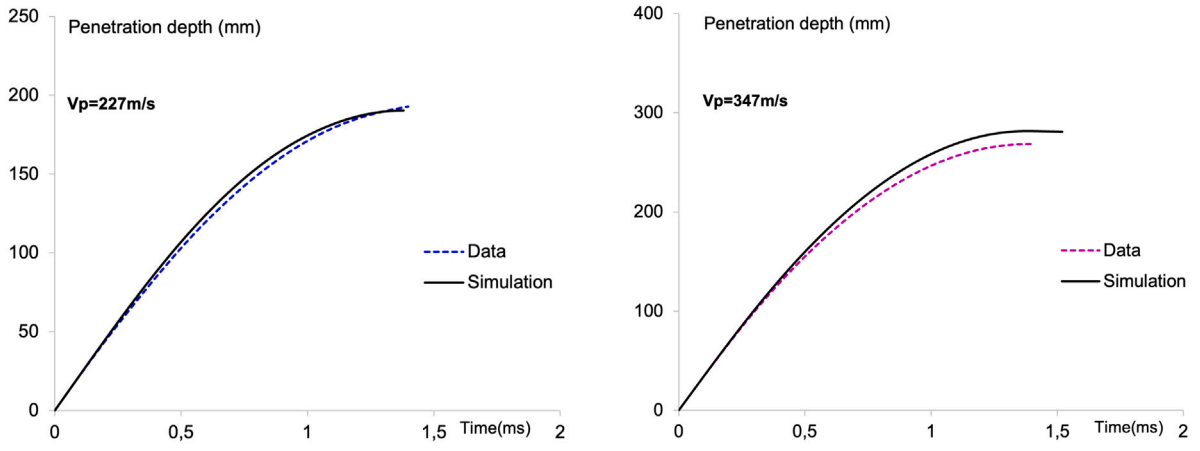

(a) $V_p = 227$ m/s (b) $V_p = 347$ m/s

Fig. 8. Penetration depth versus time in the penetration tests of saturated concrete targets.

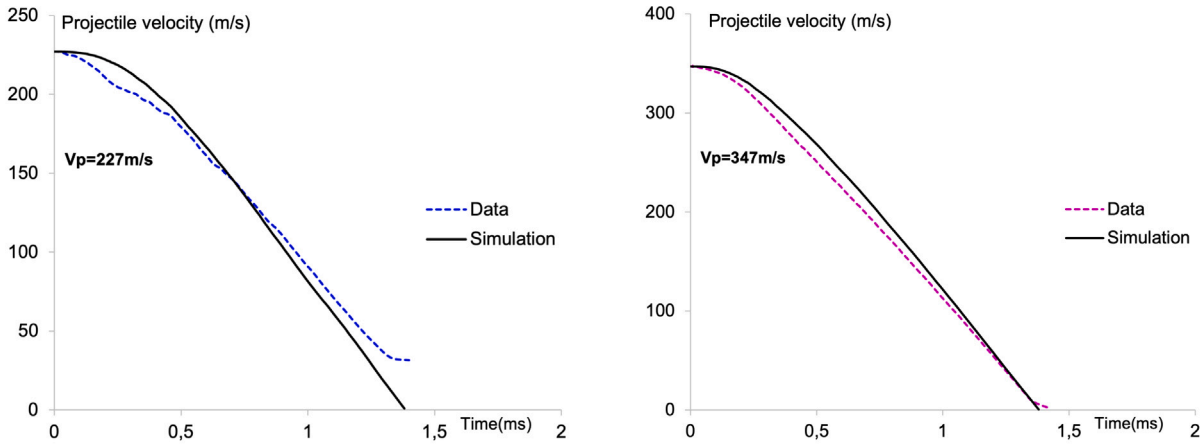

(a) $V_p = 227$ m/s (b) $V_p = 347$ m/s

Fig. 9. Projectile velocity versus time in the penetration tests of saturated concrete targets.

a constant value (p_w^{max} = 136 MPa at t = 0.8 ms; p_w^{max} = 147 MPa at t = 1.2 ms) and finally decreases with the projectile deceleration (p_w^{max} = 105 MPa at t = 1.5 ms). The results of penetration test with V_p = 347 m/s are shown in Fig. 11. At the beginning of penetration phase, higher pressure is observed compared to the test with V_p = 227 m/s, with p_w^{max} = 186 MPa at t = 0.1 ms. As the projectile decelerates more strongly in the test with V_p = 347 m/s, one observes that the projectile is already in the tunnelling phase at t = 0.4 ms and a stable pore pressure is observed from t = 0.4 ms to t = 1.2 ms: p_w^{max} = 205 MPa at t = 0.4 ms; p_w^{max} = 223 MPa at t = 1.2 ms. After that, the interstitial pressure decreases progressively as the projectile comes to a rapid strop : p_w^{max} = 108 MPa at t = 2 ms. For the dimension of overpressure zone, it increases progressively with the penetration of projectile into the concrete target and continues to propagate gradually after the projectile stop (i.e., after 1.5 ms), indicating a hydromechanical equilibration of the concrete target.

Based on the numerical results, we can conclude that the adopted constitutive model and method provide accurate prediction of the penetration performance of saturated concrete and the projectile deceleration. Additionally, the evolution of pore water in the concrete target is quantitatively predicted by the numerical results. According to the primary objective of the present work, it is to evaluate the feasibility of employing a constitutive model, derived from static laboratory tests, for the numerical analysis of the coupled hydro-mechanical phenomena observed in dynamic tests. In the next section, the influence of strain rate on the penetration performance of concrete will be discussed by comparing the previous results with those of $DIF_{S_w}^c$ = 1, indicating the application of a static constitutive model.

4.3. Partial discussion on the influence of strain rate

The numerical results of penetration tests with and without the effects of strain rate will be compared in this section to illustrate the effects of strain rate on the penetration performance of concrete structures. The previously obtained numerical results are regrouped in two cases : Case D1 with V_p = 227 m/s and Case D2 with V_p = 347 m/s, both using the proposed constitutive model presented in the Section 2 (Table 1). Additionally, two other cases without considering the effects of strain rate (i.e. $DIF_{S_w}^c$ = 1) are performed, referred to as Case S1 for V_p = 227 m/s and case S2 for V_p = 347 m/s.

The comparisons of projectile deceleration and penetration depth are shown in Fig. 12. A higher deceleration of the projectile is observed at the beginning of Case D1, where the increase in strain rate leads to a higher yield stress limit of pore collapse. Additionally, during the tunnelling phase of Case D1, a higher projectile deceleration is observed. This can be explained by the fact that the stronger the resistance of concrete, the more difficult it is to penetrate. Moreover, a greater difference

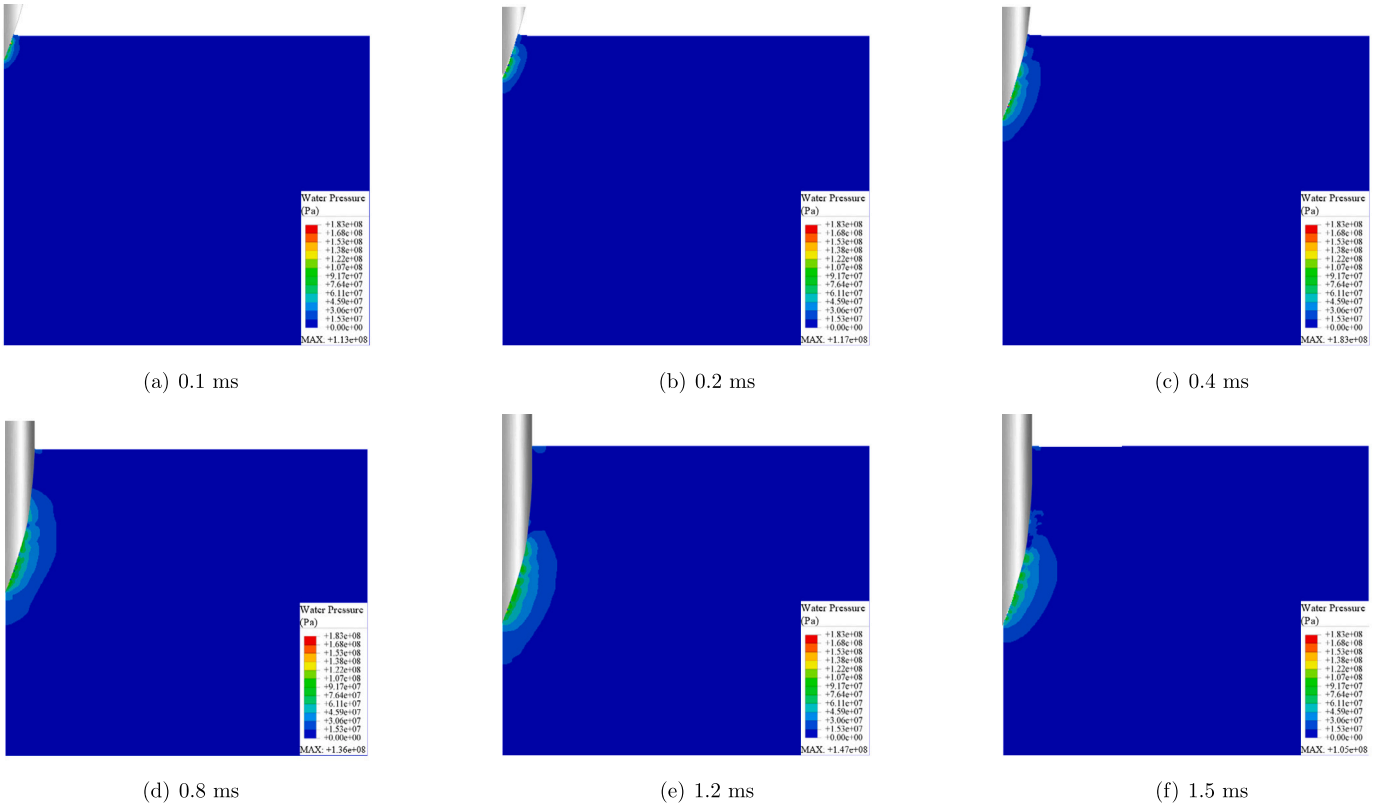

(a) 0.1 ms (b) 0.2 ms (c) 0.4 ms

(d) 0.8 ms (e) 1.2 ms (f) 1.5 ms

Fig. 10. Distribution of water pressure in the saturated concrete target at different instants in the penetration test with $V_p = 227$ m/s (Case D1).

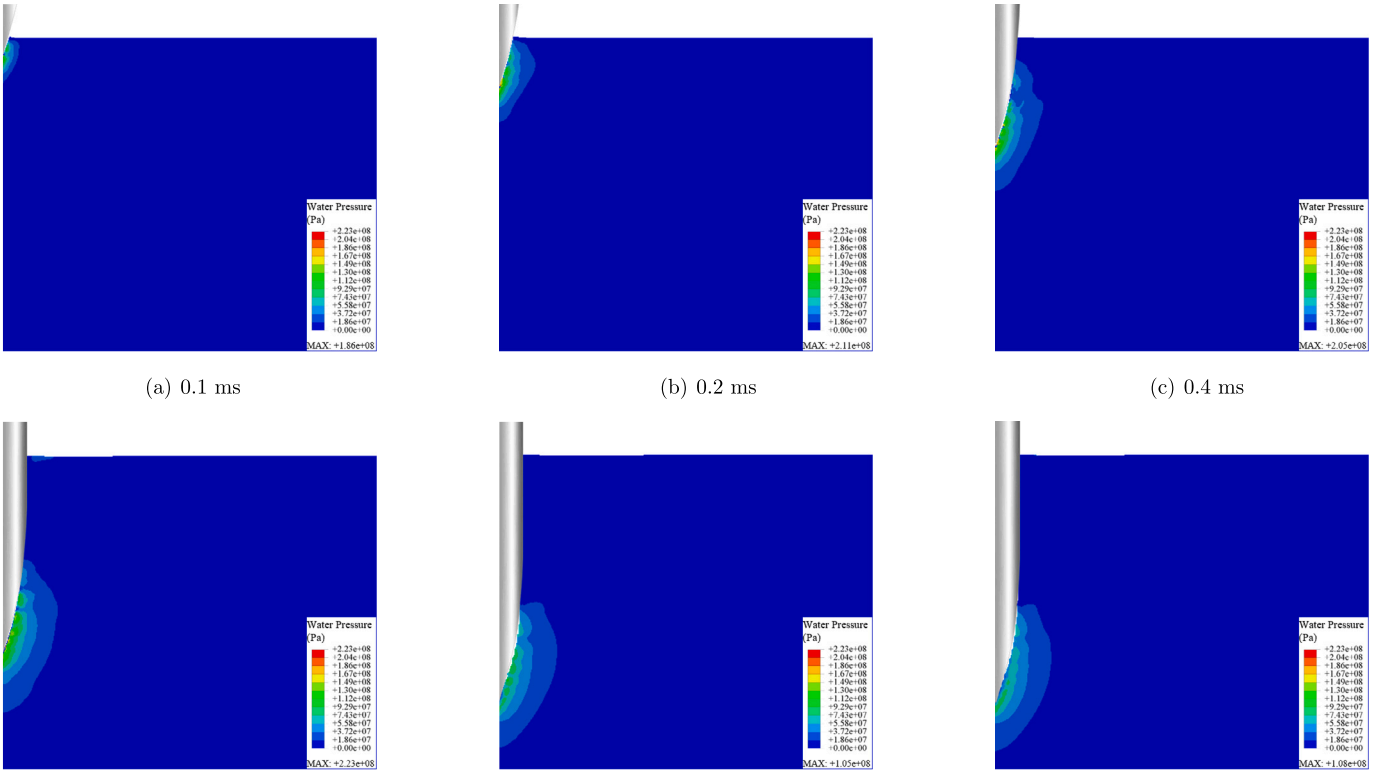

(a) 0.1 ms (b) 0.2 ms (c) 0.4 ms

(d) 0.8 ms (e) 1.5 ms (f) 2.0 ms

Fig. 11. Distribution of water pressure in the saturated concrete target at different instants in the penetration test with $V_p = 347$ m/s (Case D2).

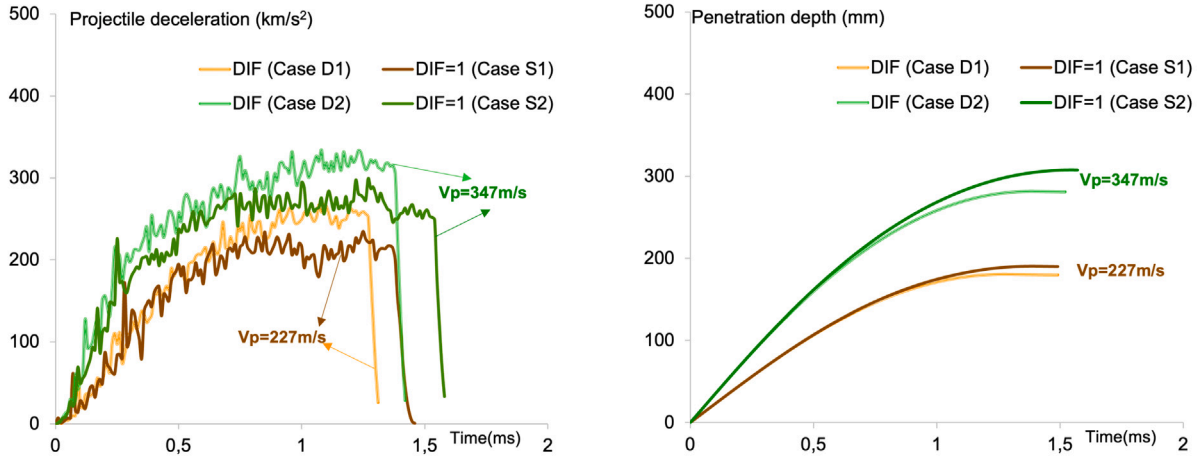

(a) Projectile deceleration (b) Penetration depth

Fig. 12. Influence of strain rate on the projectile deceleration and penetration depth in the penetration tests of saturated concrete targets with $V_p = 227$ m/s and 347 m/s.

in penetration depth and projectile deceleration is observed between the Cases D2 and S2 compared to those with a lower V_p (Cases D1 and S1). This observation is due to the fact that with the increase of initial projectile velocity, the effects of strain rate becomes more important. The distributions of interstitial pressure in the penetration test with $V_p = 227$ m/s (Case S1), without considering the effects of strain rate, are given at six different moments (Fig. 13). As previously mentioned, an important overpressure is also observed around the tunnel field of projectile trajectory and this overpressure zone develop progressively into the target with the projectile penetration. The maximum value of overpressure (p_w^{max}) initially increases with the projectile penetration, then tends to stabilize towards a constant value ($p_w^{max} = 168$ MPa at $t = 0.2$ ms; $p_w^{max} = 173$ MPa at $t = 0.4$ ms; $p_w^{max} = 168$ MPa at $t = 1.2$ ms) and finally decreases with the projectile deceleration ($p_w^{max} = 89$ MPa at $t = 1.5$ ms). However, the obtained values of water pressure are generally smaller than those of the Case D1. In general, a similar evolution in the coupled hydro-mechanical behaviour of concrete and projectile deceleration is observed, regardless of the presence or absence of strain rate effects

In Cases S1 and S2, despite the non-consideration of strain rate effects and the slight scatter observed between the experimental data and numerical results, the general trend of projectile velocity evolution has been correctly reproduced. Furthermore, the numerical results of cases S1 and S2 are capable of capturing the effects of projectile velocity, as well as the coupled hydro-mechanical behaviour of concrete subjected to the penetration of a rigid projectile. Based on these numerical results, we can conclude that the main features observed in the penetration test can be reproduced using a constitutive model derived from static experimental tests. Moreover, the influence of strain rate on the behaviour of concrete with different water saturation levels remains an ongoing research topic. Since the present work focuses on the coupled hydro-mechanical behaviour of concrete under impact loads, the static constitutive model (with $DIF^c_{S_w} = 1$) will be employed to study the response of unsaturated and saturated concretes subjected to projectile penetration in the next section. The influence of water saturation on the penetration performance of concrete will also be discussed.

5. Projectile penetration tests performed on unsaturated concrete targets

Inspired on the previous parametric study, the penetration tests are simulated using the static constitutive model ($DIF^c_{S_w} = 1$) and a new limit value for erosion criterion ($\gamma^p_{\max} = 3$), which is obtained by best fitting the experimental results of the penetration test with $V_p = 227$ m/s (Case 1). To address the principal objective of the present study, the penetration preformation of concrete targets with different S_w is analysed using $DIF^c_{S_w} = 1$ and $\gamma^p_{\max} = 3$ (Table 1).

Due to the dimensions of target (with a radius of 40 cm and a height of 80 cm) and low permeability of concrete, the total drying of concrete target to a desired S_w will take a very long time and then no dry/unsaturated target is available for the realization of penetration test in the laboratory. As a result, the penetration performance of dry concrete and two partially saturated concretes ($S_w = 80\%$ and 60%) are numerically investigated in this section. The dry targets are numerically reproduced without the consideration of interstitial pressure. For the partially saturated targets ($S_w = 80\%$ and 60%), the liquid pressures obtained by Eq. (6) are taken as the initial values. The numerical results of unsaturated concrete targets will be compared with those of saturated ones (cases 1 and 2) to analyse the influence of water saturation on the penetration performance of concrete targets.

5.1. Evolution of projectile deceleration

The deceleration-time responses of projectile in the targets with different S_w are given in Fig. 14. In general, three phases of projectile deceleration are clearly observed in the numerical results. To capture the influence of water saturation on the penetration process of projectile into concrete target, four numerical simulations with $V_p = 227$ m/s are firstly compared (Fig. 14a). It is observed that water saturation has an important impact on the projectile deceleration kinetics: the amplitude of projectile deceleration increases with decreasing S_w. Therefore, the most important projectile deceleration is observed in the dry target (Fig. 14). After that, the influence of projectile velocity V_p is discussed by using the numerical results for the same S_w. One observes that the higher projectile deceleration is always observed in the test with higher projectile velocity, i.e., $V_p = 347$ m/s. In order to quantify the influence of projectile velocity on the penetration behaviour of projectile, the mean values of penetration decelerations are compared in Fig. 15: With the increase of S_w, the difference between the results of two V_p decreases. For instance: the difference of penetration deceleration between two V_p, is equal to 34 km/s^2 for $S_w = 100\%$, 84 km/s^2 for $S_w = 80\%$, 93 km/s^2 for $S_w = 60\%$ and 97 km/s^2 for $S_w = 11\%$, respectively. The comparison of these four values shows that the smallest value is

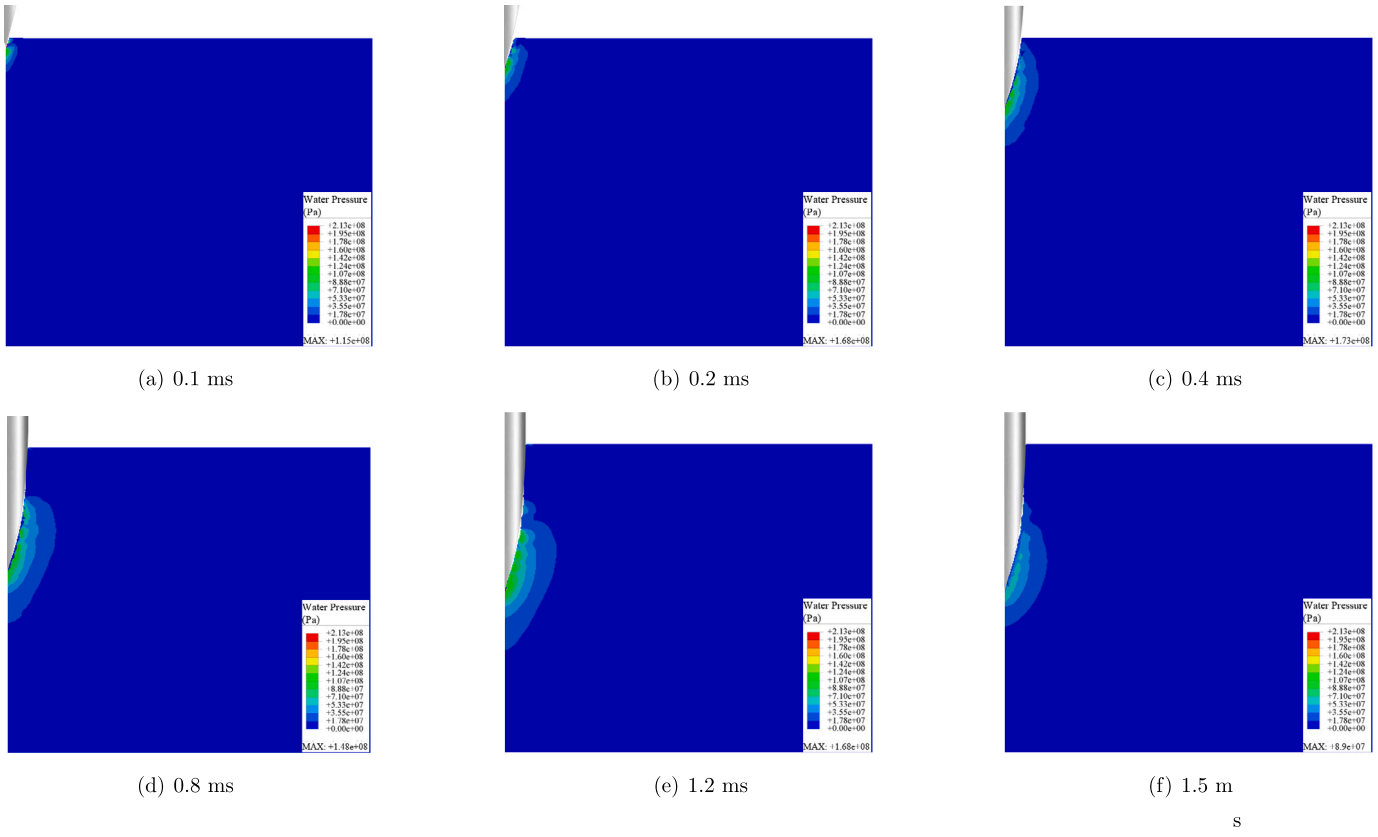

(a) 0.1 ms (b) 0.2 ms (c) 0.4 ms

(d) 0.8 ms (e) 1.2 ms (f) 1.5 ms

Fig. 13. Distribution of water pressure in the saturated concrete target at different instants in the penetration test with $V_p = 227$ m/s and $DIF^c_{S_w} = 1$ (Case S1).

obtained in the saturated case while a slight difference is observed in dry and partially saturated cases.

By comparing the tunnelling phase of projectile deceleration curves (Fig. 14), a significant influence of water saturation on the kinetics of projectile deceleration is also observed. A quasi-constant projectile deceleration is observed in the saturated target. For the dry concrete, a constant increase of projectile deceleration can be noticed. In unsaturated concretes (S_w = 80%, 60%), their deceleration evolutions of projectile are similar initially until a constant value is reached in a subsequent phase. These observations may be related to the presence of air in the pores of unsaturated/dry concretes and the dependence of material strength/behaviour on the water saturation. Under the high-intensity stress from projectile penetration, air in the pores of unsaturated concretes can be easily compressed, leading to significant pore collapse. In contrast, in saturated samples, where pores are filled with almost incompressible water, substantial overpressure develops around the projectile trajectory, resulting in a marked decrease in effective stress on the solid skeleton. Moreover, the strength of saturated concrete is less sensitive to the increase of applied stress with respect to the dry and partially saturated ones (Fig. 1b).

5.2. Evolution of projectile velocity

The evolutions of projectile velocity are given in Fig. 16. We begin with the numerical results of V_p = 237 m/s. The smaller S_w is, the more important projectile deceleration is (Fig. 16). As a result, the duration of projectile penetration decreases with decreasing of water saturation. For instance, in the tests with V_p = 347 m/s, the projectile is stopped at 1.73 ms for S_w = 100%, 1.4 ms for S_w = 80%, 1.35 ms for S_w = 60%, and 1.16 ms for dry concrete. Again, it is observed that the influence of projectile velocity is accentuated by the increase of water saturation. For instance: the penetration duration of projectile with V_p = 347 m/s is longer than that of V_p = 227 m/s about 0.27 ms for S_w = 100%, 0.14 ms for S_w = 80%, 0.12 ms for S_w = 60%, and 0.08 ms for dry concrete. This difference may be also related to two phenomena: Firstly, under high confining pressures, the failure strength of saturated concrete tends to a constant while that of unsaturated concretes increases progressively with increasing confining pressure. Secondly, more important pore collapse is developed in dry target, with respect to the fully/partially saturated one.

5.3. Evolution of penetration depth

The curves of penetration depth are compared in Fig. 17. For a given V_p, it is noted that at the beginning of penetration tests, the same curve is observed in the tests with different S_w. With the progressive penetration of projectile into the concrete target, the effects of water saturation become clear and different penetration depths are obtained at the end of tests : the final penetration depth increases when S_w increases (Fig. 15b). The influence of projectile velocity is also studied. In order to quantify the influence of V_p on the penetration depth at different levels of S_w, the difference of penetration depth between two tests with different V_p is discussed and compared: 137 mm for S_w = 100%, 108 mm for S_w = 80%, 98 mm for S_w = 60% and 88 mm for S_w = 11%, respectively. This observation can be explained by the dependence of failure strength on the degree of water saturation, the effective stress applied on solid skeleton and the presence air/water in the pores. Under high confining pressures, the failure strength of dry and partially saturated concretes increase progressively with the increase of mechanical loading while the failure strength of saturated

concrete increases very slightly and tends to converge towards a constant (Fig. 1b). When the concrete target is penetrated by a rigid projectile, a higher projectile velocity results in a more high-intensity stress state in concrete target [47]. As a result, unsaturated concretes exhibit a more important increase of failure strength in the test with V_p = 347 m/s with respect to the saturated ones. Consequently, a higher projectile deceleration response is observed in the target with smaller S_w and induces a smaller increase of penetration depth when V_p increases from 227 m/s to 347 m/s. Moreover, in saturated targets, the induced high-intensity stress is carried by both pore water and solid skeleton while it is partially/only supported by the solid skeleton phase in partially saturated/dry concretes. Additionally, free water lubricates the spaces between concrete and projectile, reducing viscous friction and then facilitate the penetration of projectile in the concrete target. As a result, the most important pore collapse is observed in unsaturated samples, which prevents the projectile penetration. As a result, the biggest difference of penetration depth in the tests with two V_p is obtained in saturated samples.

5.4. Evolution of interstitial pressure

The evolutions of interstitial pressure in unsaturated concrete target are given in Fig. 18. An overpressure zone is also observed around the projectile trajectory and advances progressively with the projectile penetration. In general, one observes that the maximum interstitial pressure obtained in the sample decreases with increasing water saturation, while the dimension of overpressure zone increases with decreasing water saturation. For instance: at t = 0.1 ms, p_w^{max} = 180 MPa for S_w = 60% and p_w^{max} = 116 MPa for S_w = 100%; at t = 0.4 ms, p_w^{max} = 297 MPa for S_w = 60% and p_w^{max} = 180 MPa for S_w = 100%. These observations may be related to the presence of air in the unsaturated concrete (S_w = 60%) and important pore collapse obtained in the sample. As a result, higher interstitial pressure occurs in the unsaturated sample (S_w = 60%) with respected to the saturated one. With the combination of pore collapse and volumetric compaction induced by the high-intensity stress, the unsaturated sample is saturated progressively around the projectile trajectory while the other part keeps its initial value of S_w and seems to be undisturbed by the projectile penetration.

The variations of interstitial pressure Δp_w at two points (A, B) located on the line $x = 0.7R$ are given in Fig. 20a. The distances between the upper surface of concrete target and the points A, B are equal to 50 mm and 100 mm, respectively. In general, three successive phases are observed in different curves of Δp_w : a rapid increase phase, a steady phase and a rapid decrease phase. This observation is consistent with three phases of projectile deceleration. For the point A, the comparison of three curves of Δp_w shows that the increasing amplitude of Δp_w increases with decreasing degree of water saturation and the biggest Δp_w is observed in the case with the smallest S_w (i.e., S_w = 60%). The same phenomenon is observed in three curves of point B. These phenomena are related to the volumetric compaction of concrete targets: the most important Δp_w is obtained in the case of S_w = 60%, where the largest number of pores are filled with air. For a given S_w, two curves of points (A, B) are compared. One observes that the values of Δp_w at the point A are generally smaller than those of the point B. This observation is coherent with the rapid increase of interstitial pressure during the penetration phase.

On the other hand, two points C, D, located at the line $x = 1.5R$ are presented in Fig. 20b. Three phases are also observed in two curves of saturated concrete. However, rapid increase or decrease of Δp_w is no more observed and Δp_w increases/decreases progressively with the projectile penetration/deceleration. Moreover, Δp_w of the point D is higher than that of the point C, which is closer to the upper surface of target than D. These observations are due to the fact that the high-intensity stress increases progressively with the projectile penetration. Moreover, in the unsaturated sample with S_w = 80%, the higher Δp_w is obtained at the point C with respected to the point D, where the evolution of Δp_w is almost undisturbed by the projectile penetration. Moreover, for the sample with S_w = 60%, the evolutions of Δp_w at two points C, D are almost independent on the projectile penetration. Again, the numerical results exhibit that water saturation of concrete has an important impact on the response of target subjected to the penetration of a rigid projectile: the dimension of overpressure zone decreases with decreasing water saturation and the evolution of interstitial pressure Δp_w depends on both the saturation state of concrete target and the distance between the projectile trajectory and studied zone/point.

Generally, with the decrease of water saturation, the projectile deceleration increases and the penetration depth decreases. Moreover, the influence of projectile velocity on the penetration behaviour of projectile increases with increasing water saturation of concrete. These numerical results allow us to get a quantitative estimation of the influence of water saturation on the penetration performance of concrete targets. In conclusion, the projectile penetration process depends strongly on the water saturation of concrete structure (see Fig. 19).

5.5. Discussions

To illustrate the importance of a coupled hydro-mechanical modelling of penetration performance of concrete targets, two penetration tests performed on saturated concrete targets are recalculated using the same parameters without the consideration of interstitial pressure, called numerically dry cases (i.e. Cases 3 and 4) in Table 1. The numerical results of penetration tests, with and without interstitial pressure p_w, are compared in Figs. 21 and 22. One observes that the influence of interstitial pressure is clearly identified: for a given V_p, a more important projectile deceleration is observed in the numerically dry concrete (p_w = 0). This observation is related to the fact that in saturated concrete, the volume decrease creates an increase of interstitial pressure and then induces a decrease of effective stress applied on the solid skeleton. As a result, the projectile is decelerated more rapidly in numerical dry concrete (p_w = 0) and a smaller penetration depth is then obtained. On the other hand, for a given V_p, it is observed that the influence of projectile velocity on the penetration response of concrete target is amplified by the presence of free water. For instance: the difference between the mean values of projectile deceleration of saturated target and that of numerically dry case is equal to 22 km/s^2 for V_p = 227 m/s and 43 km/s^2 for V_p = 347 m/s while the difference of the corresponding penetration depth is about 20 mm for V_p = 227 m/s and about 56 mm for V_p = 347 m/s. Theses observations are coherent with the experimental observations [33]. Based on the previous results, we can conclude that the mechanical behaviour of concrete is strongly coupled with its hydraulic response. To get a good evaluation of structure safety, it is necessary to take into account the influence of interstitial pressure and perform a coupled hydromechanical modelling in the penetration tests.

There are several, occasionally conflicting, mechanisms that can explain the sensitivity of strength to water content. Firstly, the skeleton is strengthened by the surface tension of the air/water interface layer within the material because of the capillary suction effects [26, 71]. Meanwhile, concrete strength decreases as the degree of saturation increases due to the decrease of capillary suction. Secondly, water acts as a wedge in fracture. Under static/quasi-static loading conditions, water gradually fills the meniscus, the tip of the crack, creating a point of stress concentration where the crack propagates and weakens saturated samples. On the other hand, free water rushes to expand/push out of cracks quickly under dynamic loading, which results in a strength increase since it does not have enough time to build stress concentration at the crack tip [7]. Thirdly, free water lubricates the spaces between the material's cracks, reducing viscous friction and then weakening the porous media [72]. Fourthly, the Stephan effects produce a response force on the plates according to the separation velocity when a viscous liquid is trapped between two rapidly separating plates [73]. Fifthly, the concrete strength increases with the applied

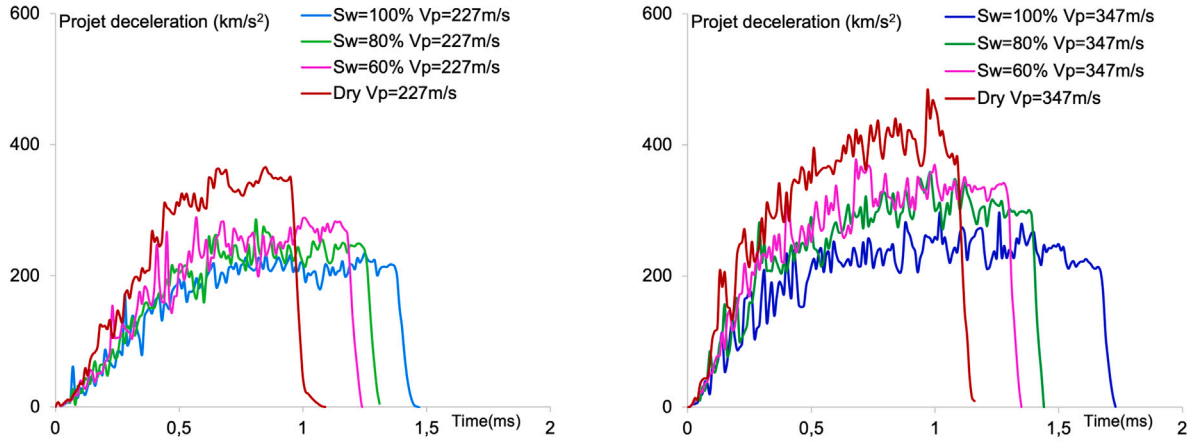

(a) $V_p = 227$ m/s (b) $V_p = 347$ m/s

Fig. 14. Projectile velocity versus time in the penetration tests with different S_w.

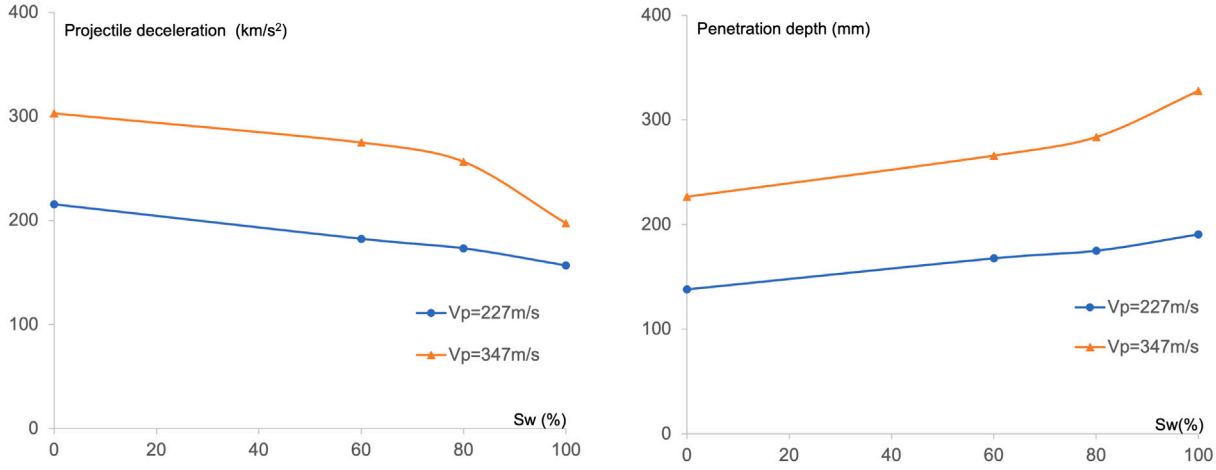

(a) Mean value of projectile deceleration (b) Penatration depth

Fig. 15. Comparison of numerical results with different S_w.

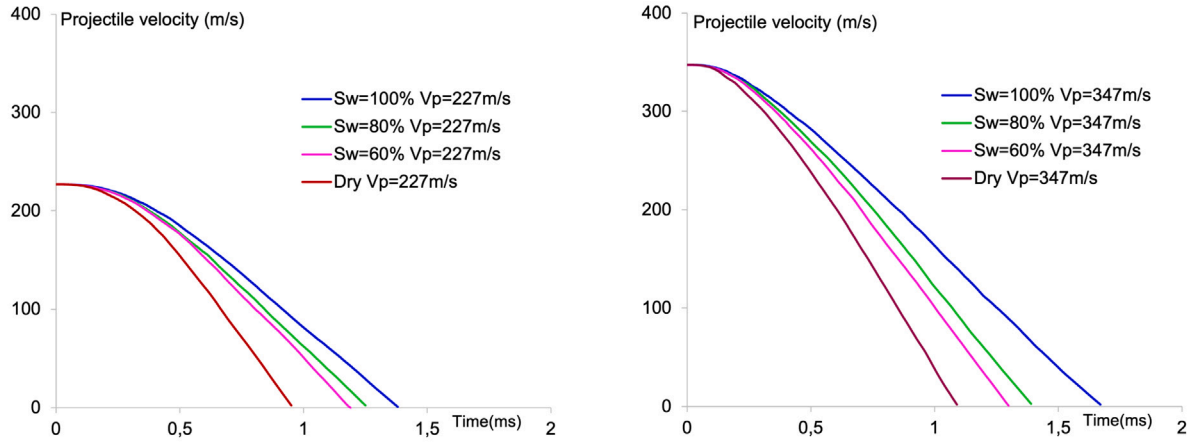

(a) $V_p = 227$ m/s (b) $V_p = 347$ m/s

Fig. 16. Projectile velocity versus time in the penetration tests with different S_w.

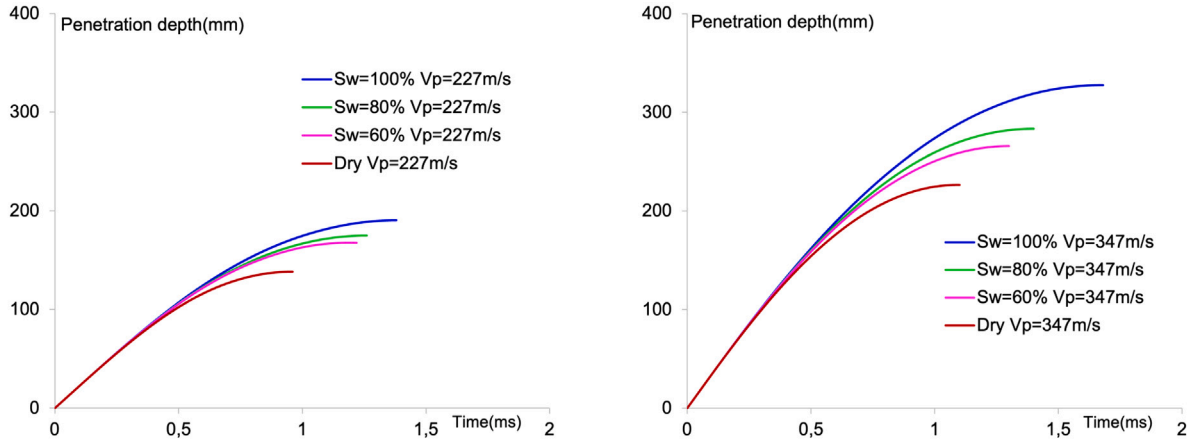

(a) $V_p = 227$ m/s (b) $V_p = 347$ m/s

Fig. 17. Comparison of numerical results with different S_w.

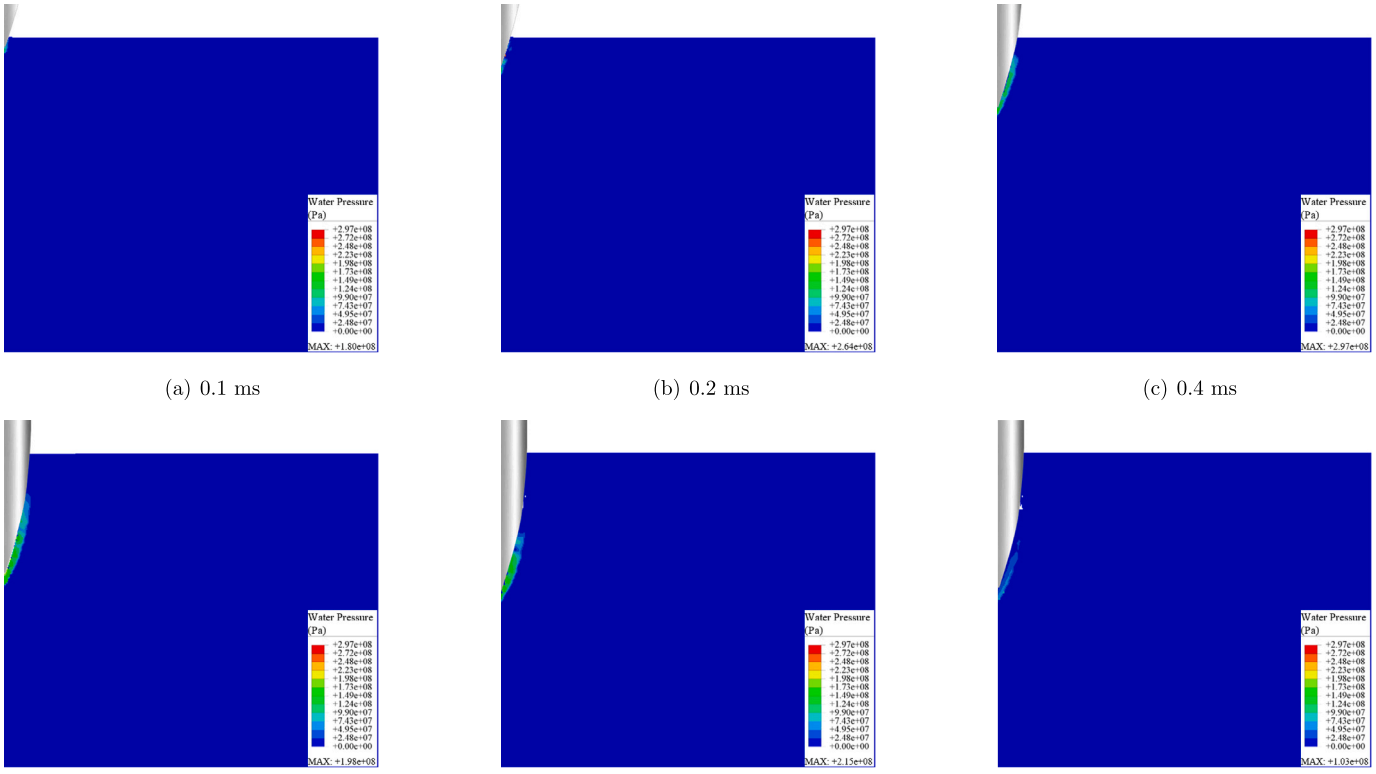

(a) 0.1 ms (b) 0.2 ms (c) 0.4 ms

(d) 0.8ms (e) 1.2 ms (f) 1.5 ms

Fig. 18. Distribution of water pressure in the unsaturated concrete target ($S_w = 60\%$) at different instants in the penetration test with $V_p = 227$ m/s.

loading due to the increase in pore water pressure within the cement matrix. Some researchers refer to this phenomenon as restricting effects [17]. However, this pressure increase within gel pores, observed in some experiments [19,21,35,74], potentially induces split-tensile force and further degrades material strength. Finally, the strength of a wet concrete may be degraded by moisture and temperature-induced expansion, which may create internal stress on certain components of concrete, such as olivine, pyroxenes and quartz [47].

6. Conclusions

In the present work, an elastoplastic model is improved to describe the influence of water saturation on the penetration performance of concrete structures. The modified model is then verified by comparison with the experimental data at material and structure scales. A series of parametric studies are performed to investigate the influence of water saturation on the penetration performance of concrete targets subjected to a rigid projectile. The conclusions are summarized as follows:

(I). Water saturation of concrete has an important impact on the penetration performance of concrete structures due to the dependence of failure strength on water saturation, the induced pores closure, the interstitial pressure and the presence of free water;

(II). During the penetration of a projectile in a concrete target, target with lower saturation degree exhibits higher penetration resistance, indicating a smaller penetration depth and a more important projectile deceleration;

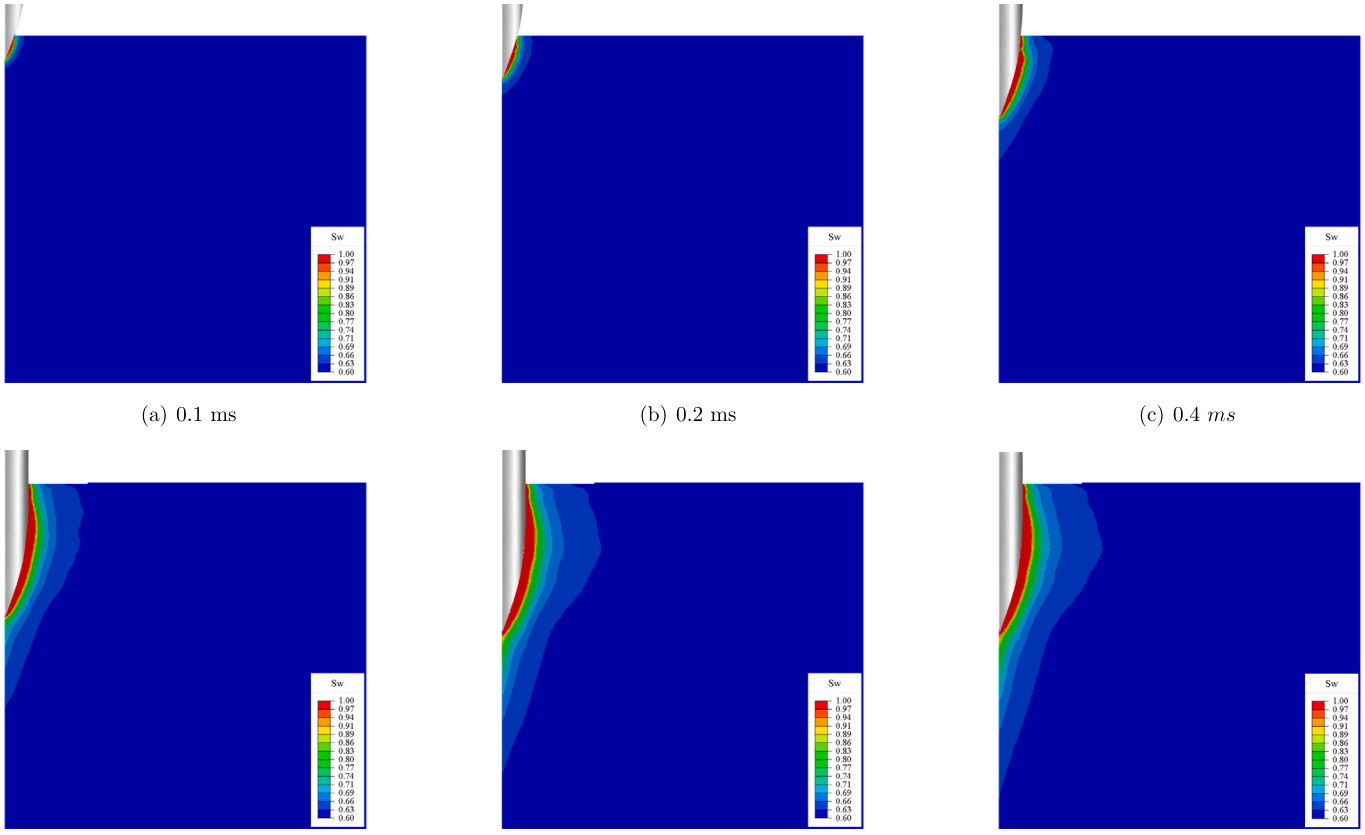

(a) 0.1 ms (b) 0.2 ms (c) 0.4 ms

(d) 0.8 ms (e) 1.2 ms (f) 1.5 ms

Fig. 19. Distribution of water saturation in the unsaturated concrete target ($S_w = 60\%$) at different instants in the penetration test with $V_p = 227$ m/s.

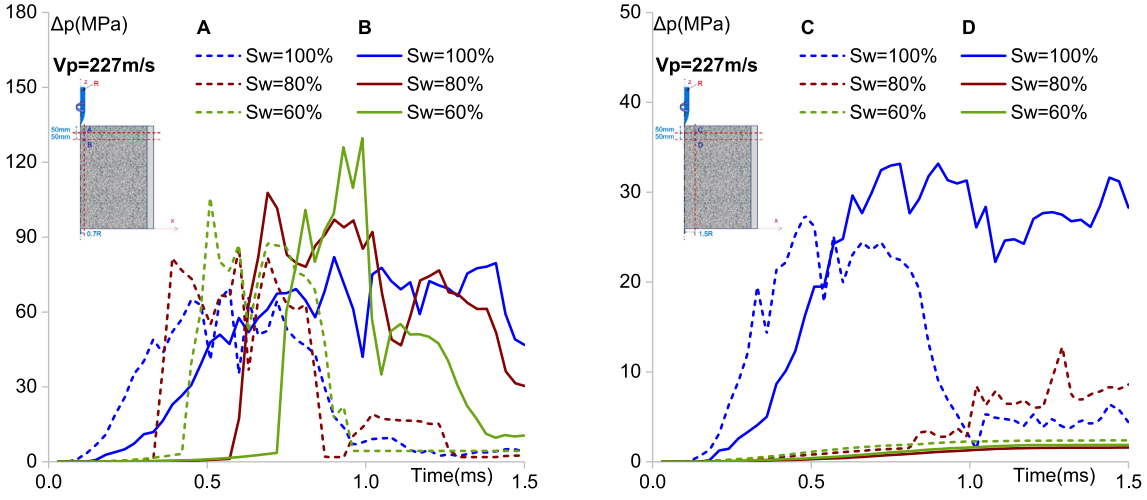

(a) $x = 0.7R$ (b) $x = 1.5R$

Fig. 20. Projectile velocity versus time in the penetration tests with different S_w.

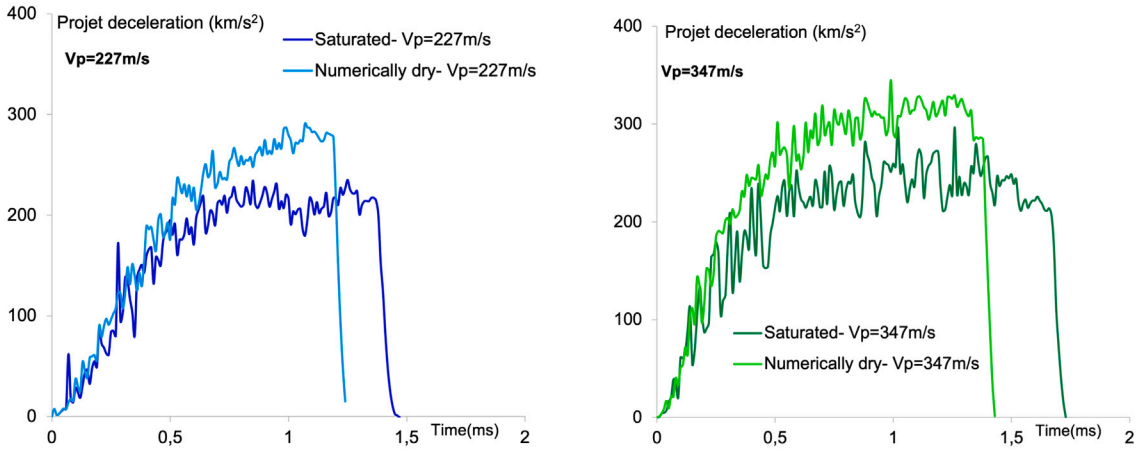

(a) $V_p = 227$ m/s (b) $V_p = 347$ m/s

Fig. 21. Influence of interstitial pressure p_w on the projectile deceleration in saturated targets.

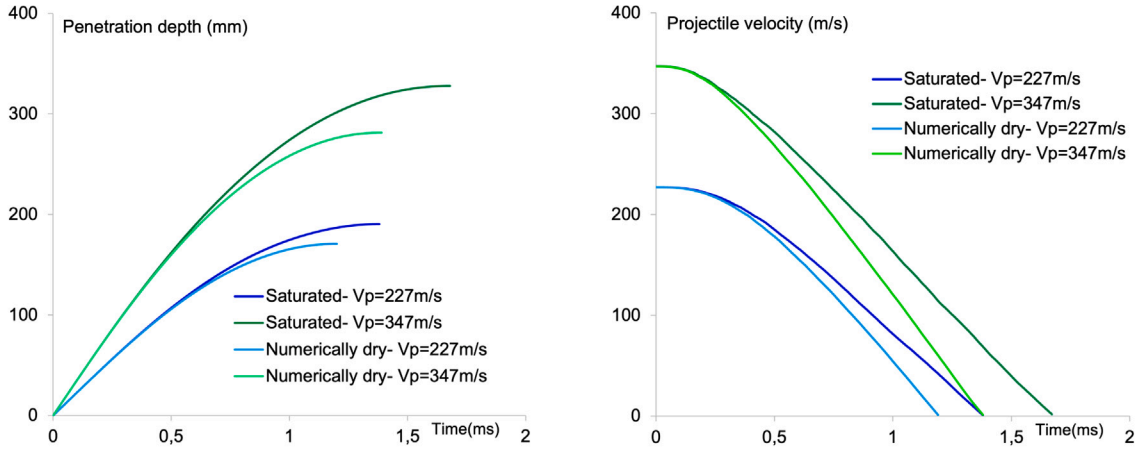

(a) Penatration depth (b) Projectile velocity

Fig. 22. Influence of interstitial pressure p_w on the numerical results of saturated targets.

(III). Concerning the interstitial pressure, an important overpressure zone is observed around the penetration trajectory and advances progressively into the target during the penetration process of projectile : the dimension of overpressure zone decreases with decreasing water saturation;

(IV). The evolution of interstitial pressure in concrete structure depends on both the saturation state of concrete and the distance between the projectile trajectory and the studied zone/point;

(V). The influence of projectile velocity on the penetration performance of concrete target is accentuated with the increase of water saturation and the presence of pore water.

The present study is capable of providing a quantitative estimation of hydro-mechanical behaviour of concrete target subjected to a rigid projectile. The vulnerability of concrete structures subjected to near-field impacts requires a good understanding of the coupled hydro-mechanical behaviour of concrete. Moreover, numerical modelling and analysis will enhance our understanding of the vulnerability of concrete infrastructure subjected to near-field detonations or impacts. By incorporating the influence of strain rate on concrete behaviour through a semi-empirical function, the present work represents the first series of numerical results on the hydro-mechanical behaviour of saturated and unsaturated concretes under projectile impacts. Future numerical simulations will be performed by incorporating more detailed effects of strain rate in penetration tests.

Nomenclature

$d\underline{\underline{\varepsilon}}$	Total strain tensor
$d\underline{\underline{\varepsilon}}^e$	Elastic strain tensor
$d\underline{\underline{\varepsilon}}^p$	Plastic strain tensor
p_g	Pressure of gas mixture
p_{va}	Pressure of vapour
p_{da}	Pressure of dry air
p_w	Water pressure
p_{cp}	Capillary pressure
$d\pi$	Equivalent pore pressure
S_w	Water saturation degree
K_b	Drained bulk modulus
G	Shear modulus
ϵ_v^e	Elastic volumetric strain
$\underline{\underline{\delta}}$	Second-order unit tensor
M_{ww}	Biot's modulus
b	Biot's coefficient
ϕ	Porosity
K_s	Bulk modulus of solid matrix
K_w	Compressibility modulus of liquid water
$\underline{\underline{\sigma'}}$	Net stress tensor

$\underline{\underline{\mathrm{d}\varepsilon^{ps}}}$	Shear plastic part
$\underline{\underline{\mathrm{d}\varepsilon^{pc}}}$	Plastic pore collapse part
$\mathrm{d}\phi^{p}$	Porosity variation
F_c	Yield function for pore collapse plasticity
p	Mean net stress
q	Deviatoric net stress
$\bar{\sigma}$	Plastic yield stress of concrete solid matrix
$\underline{\underline{s'}}$	Deviatoric stress tensor
ε_M^{pc}	Plastic volumetric strain due to pore collapse
$\bar{\sigma}_0$	Initial yield stress of the solid matrix
a, n, β	Three hardening law parameters for pore collapse plasticity
n_s	Asymptotic value of n for saturated concrete
n_d	Asymptotic value of n for dry concrete
ξ_n	Parameter controlling the evolution n in function of S_w
Q_c	Plastique potential function for pore collapse plasticity
F_s	Yield function of shear plasticity
γ^{ps}	Shear plastic distortion
α_s	Hardening law of shear plasticity
p_r	Reference pressure
c_1	Equivalent friction coefficient
c_3	Cohesion coefficient
c_2	Nonlinearity of yield surface for shear plasticity
ξ_{c2}	Parameter controlling the evolution c_2 in function of S_w
c_{2s}	Value of c_2 for saturated concrete
c_{2d}	Value of c_2 for dry concrete
α_s^0	Initial yielding threshold of shear plasticity
ζ	Parameter controlling the plastic hardening rate
$\underline{\underline{\delta}}$	Second order unit tensor
η	Slope of the boundary between contractive and dilatant zones
I_0	Intersection of the plastic potential surface with the p axis
$\mathrm{d}\phi^{ps}$	Porosity related to shear plasticity
$\mathrm{d}\phi^{pc}$	Porosity related to pore collapse plasticity
$d\lambda_c$	Plastic multiplier for pore collapse plasticity
$d\lambda_s$	Plastic multiplier for shear plasticity
$\underline{\underline{\underline{\underline{C}}}}$	Elastic stiffness tensor
K	Bulk modulus
df_c, df_s	Plastic consistency conditions
$\underline{\underline{\underline{\underline{I}}}}$	Symmetric fourth order unit tensor
V_p	Velocity of projectile
γ_{max}^{p}	Equivalent plastic deformation for the erosion criterion
f	Friction coefficient
Δp_w	Variations of interstitial pressure

CRediT authorship contribution statement

Yun Jia: Writing – original draft, Validation, Methodology, Conceptualization. **Yudan Jin:** Writing – review & editing, Visualization, Data curation. **Hanbing Bian:** Writing – review & editing, Supervision, Software, Resources, Methodology, Investigation, Conceptualization. **Wei Wang:** Writing – review & editing, Visualization, Software. **Jianfu Shao:** Writing – review & editing, Supervision, Conceptualization.

Declaration of competing interest

The authors declare that they have no known competing financial interests or personal relationships that could have appeared to influence the work reported in this paper.

Data availability

No data was used for the research described in the article.

Acknowledgments

The numerical simulations in this paper have been done on the HPC Computing Méso-centre of University of Lille. The authors gratefully thank the anonymous reviewers for their constructive comments as well.

References

[1] Forrestal M, Frew D, Hanchak S, Brar N. Penetration of grout and concrete targets with ogive-nose steel projectiles. Int J Impact Eng 1996;18(5):465–76.
[2] Daudeville L, Malécot Y. Concrete structures under impact. Eur J Environ Civ Eng 2011;15(sup1):101–40.
[3] Kong X, Wu H, Fang Q, Zhang W, Xiao Y. Projectile penetration into mortar targets with a broad range of striking velocities: Test and analyses. Int J Impact Eng 2017;106:18–29.
[4] Liu J, Wu C, Su Y, Li J, Shao R, Chen G, Liu Z. Experimental and numerical studies of ultra-high performance concrete targets against high-velocity projectile impacts. Eng Struct 2018;173:166–79.
[5] Huang X-p, Hu J, Zhang X-d, Zhang Z-t, Kong X-z. Bending failure of a concrete gravity dam subjected to underwater explosion. J Zhejiang Univ-Sci A 2020;21(12):976–91.
[6] Baranowski P, Kucewicz M, Małachowski J, Sielicki PW. Failure behavior of a concrete slab perforated by a deformable bullet. Eng Struct 2021;245:112832.
[7] Gabet T, Malécot Y, Daudeville L. Triaxial behaviour of concrete under high stresses: Influence of the loading path on compaction and limit states. Cem Concr Res 2008;38(3):403–12.
[8] Vu XH, Malecot Y, Daudeville L, Buzaud E. Experimental analysis of concrete behavior under high confinement: Effect of the saturation ratio. Int J Solids Struct 2009;46(5):1105–20.
[9] Malecot Y, Daudeville L, Dupray F, Poinard C, Buzaud E. Strength and damage of concrete under high triaxial loading. Eur J Environ Civ Eng 2010;14(6–7):777–803.
[10] Selyutina N, Petrov YV. The water-saturation effect for concretes and rocks subjected to high strain rates. Procedia Struct Integr 2018;13:705–9.
[11] Malecot Y, Zingg L, Briffaut M, Baroth J. Influence of free water on concrete triaxial behavior: The effect of porosity. Cem Concr Res 2019;120:207–16.
[12] Bazant ZP, Bishop FC, Chang T-P, et al. Confined compression tests of cement paste and concrete up to 300 ksi. ACI J 1986;33(1986):553–60.
[13] Burlion N, Pijaudier-Cabot G, Dahan N. Experimental analysis of compaction of concrete and mortar. Int J Numer Anal Methods Geomech 2001;25(15):1467–86.
[14] Forquin P, Safa K, Gary G. Influence of free water on the quasi-static and dynamic strength of concrete in confined compression tests. Cem Concr Res 2010;40(2):321–33.
[15] Erzar B, Forquin P. Free water influence on the dynamic tensile behaviour of concrete. In: Applied mechanics and materials. Vol. 82, Trans Tech Publ; 2011, p. 45–50.
[16] Piotrowska E, Forquin P. Experimental investigation of the confined behavior of dry and wet high-strength concrete: quasi static versus dynamic loading. J Dyn Behav Mater 2015;1(2):191–200.
[17] Zingg L, Briffaut M, Baroth J, Malecot Y. Influence of cement matrix porosity on the triaxial behaviour of concrete. Cement Concr Res 2016;80:52–9.
[18] Accary A, Daudeville L, Malecot Y. Interstitial pore pressure in concrete under high confinement pressure: measurement and modelling. In: Proceedings of the 10th international conference on fracture mechanics of concrete and concrete structures fraMCoS-X. France; 2019.
[19] Benniou H, Accary A, Malecot Y, Briffaut M, Daudeville L. Discrete element modeling of concrete under high stress level: influence of saturation ratio. Comput Part Mech 2021;8(1):157–67.
[20] Forquin P, Arias A, Zaera R. Role of porosity in controlling the mechanical and impact behaviours of cement-based materials. Int J Impact Eng 2008;35(3):133–46.
[21] Warren TL, Forquin P. Penetration of common ordinary strength water saturated concrete targets by rigid ogive-nosed steel projectiles. Int J Impact Eng 2016;90:37–45.
[22] Kristoffersen M, Pettersen JE, Aune V, Børvik T. Experimental and numerical studies on the structural response of normal strength concrete slabs subjected to blast loading. Eng Struct 2018;174:242–55.
[23] Fu Q, Zhang Z, Zhao X, Hong M, Guo B, Yuan Q, Niu D. Water saturation effect on the dynamic mechanical behaviour and scaling law effect on the dynamic strength of coral aggregate concrete. Cem Concr Compos 2021;120:104034.
[24] Blasone MC. Experimental testing and numerical modelling of the tensile and compressiondamage in ultra-high performance concrete under impact loading (Ph.D. thesis), Université Grenoble Alpes; 2021, [2020-.].
[25] Sun X, Wang H, Cheng X, Sheng Y. Effect of pore liquid viscosity on the dynamic compressive properties of concrete. Constr Build Mater 2020;231:117143. http://dx.doi.org/10.1016/j.conbuildmat.2019.117143.

[26] Wang Q, Liu Y, Peng G. Effect of water pressure on mechanical behavior of concrete under dynamic compression state. Constr Build Mater 2016;125:501–9. http://dx.doi.org/10.1016/j.conbuildmat.2016.08.058.
[27] Ren W, Xu J, Liu J, Su H. Dynamic mechanical properties of geopolymer concrete after water immersion. Ceram Int 2015;41(9, Part B):11852–60. http://dx.doi.org/10.1016/j.ceramint.2015.05.154.
[28] Le TH, Dormieux L, Jeannin L, Burlion N, Barthélémy J-F. Nonlinear behavior of matrix-inclusion composites under high confining pressure: application to concrete and mortar. C R Méc 2008;336(8):670–6.
[29] Tran V, Donze F, Marin P. Discrete element model of concrete under high confining pressure. In: Proceeding of the 7th international conference on fracture mechanics of concrete and concrete structures. Vol. 1, 2010, p. 481–6.
[30] Suchorzewski J, Tejchman J, Nitka M. Discrete element method simulations of fracture in concrete under uniaxial compression based on its real internal structure. Int J Damage Mech 2018;27(4):578–607.
[31] Zhou H, Bian HB, Jia Y, Shao J-F. Elastoplastic damage modeling the mechanical behavior of rock-like materials considering confining pressure dependency. Mech Res Commun 2013;53:1–8.
[32] Pijaudier-Cabot G, Khaddour F, Grégoire D, Ecay L. Coupled effects between damage and permeability with a view to discrete modelling. In: CONCREEP 10. 2015, p. 49–58.
[33] Forquin P, Piotrowska E, Gary G. Dynamic testing of concrete under high confined pressure. influence of saturation ratio and aggregate size. In: EPJ web of conferences. Vol. 94, EDP Sciences; 2015, p. 01071.
[34] Yang H, Jia Y, Shao J-F, Pontiroli C. Numerical analysis of concrete under a wide range of stress and with different saturation condition. Mater Struct 2015;48(1):295–306.
[35] Bian Hb, Jia Y, Pontiroli C, Shao J-F. Numerical modeling of the elastoplastic damage behavior of dry and saturated concrete targets subjected to rigid projectile penetration. Int J Numer Anal Methods Geomech 2018;42(2):312–38.
[36] Xu LY, Xu H, Wen HM. On the penetration and perforation of concrete targets struck transversely by ogival-nosed projectiles-a numerical study. Int J Impact Eng 2019;125:39–55.
[37] Jia Y, Zhao X, Bian H, Wang W, Shao J-F. Numerical modelling the influence of water content on the mechanical behaviour of concrete under high confining pressures. Mech Res Commun 2022;119:103819.
[38] Yang A, Li J, Qu H, Pan Y, Kang Y, Zhang Y. Numerical simulation of hypervelocity impact fem-sph algorithm based on large deformation of material. 2016.
[39] Flores-Johnson E, Wang S, Maggi F, El Zein A, Gan Y, Nguyen G, Shen L. Discrete element simulation of dynamic behaviour of partially saturated sand. Int J Mech Mater Des 2016;12(4):495–507.
[40] Forquin P, Sallier L, Pontiroli C. A numerical study on the influence of free water content on the ballistic performances of plain concrete targets. Mech Mater 2015;89:176–89.
[41] Zhao FQ, Wen HM. Effect of free water content on the penetration of concrete. Int J Impact Eng 2018;121:180–90.
[42] Huang Xp, Kong Xz, Hu J, Zhang Xd, Zhang Zt, Fang Q. The influence of free water content on ballistic performances of concrete targets. Int J Impact Eng 2020;139:103530.
[43] Forrestal MJ, Frew DJ, Hickerson JP, Rohwer TA. Penetration of concrete targets with deceleration-time measurements. Int J Impact Eng 2003;28(5):479–97.
[44] Frew DJ, Forrestal MJ, Cargile JD. The effect of concrete target diameter on projectile deceleration and penetration depth. Int J Impact Eng 2006;32(10):1584–94.
[45] Coussy O, Eymard R, Lassabatère T. Constitutive modeling of unsaturated drying deformable materials. J Eng Mech 1998;124(6):658–67.
[46] Coussy O. Poromechanics. John Wiley & Sons; 2004.
[47] Bian H, Jia Y, Shao J, Pontiroli C. Numerical study of a concrete target under the penetration of rigid projectile using an elastoplastic damage model. Eng Struct 2016;111:525–37.
[48] Xu H, Wen H. Semi-empirical equations for the dynamic strength enhancement of concrete-like materials. Int J Impact Eng 2013;60:76–81.
[49] Bishop AW, Blight G. Some aspects of effective stress in saturated and partly saturated soils. Geotechnique 1963;13(3):177–97.
[50] Shao J-F, Jia Y, Kondo D, Chiarelli A-S. A coupled elastoplastic damage model for semi-brittle materials and extension to unsaturated conditions. Mech Mater 2006;38(3):218–32.
[51] Alonso EE, Gens A, Josa A. A constitutive model for partially saturated soils. Géotechnique 1990;40(3):405–30.
[52] Lade PV. Elasto-plastic stress–strain theory for cohesionless soil with curved yield surfaces. Int J Solids Struct 1977;13(11):1019–35.
[53] Desai CS. A general basis for yield, failure and potential functions in plasticity. Int J Numer Anal Methods Geomech 1980;4(4):361–75.
[54] Chen W, Saleeb A. Uniaxial behavior and modeling in plasticity. Structural engineering report no. CE-STR-82-35, School of Civil Engineering, Purdue University; 1982.
[55] Cristescu N. Asme 1995 nadai lecture—plasticity of porous and particulate materials. 1996.
[56] Desai CS, Whitenack R. Review of models and the disturbed state concept for thermomechanical analysis in electronic packaging. J Electron Packag 2001;123(1):19–33.
[57] Perić D, Ayari MA. On the analytical solutions for the three-invariant cam clay model. Int J Plast 2002;18(8):1061–82.
[58] Lade PV, Kim MK. Single hardening constitutive model for soil, rock and concrete. Int J Solids Struct 1995;32(14):1963–78.
[59] Aubertin M, Li L, Simon R, Khalfi S. Formulation and application of a short-term strength criterion for isotropic rocks. Can Geotech J 1999;36(5):947–60.
[60] Khoei A, Azami A. A single cone-cap plasticity with an isotropic hardening rule for powder materials. Int J Mech Sci 2005;47(1):94–109.
[61] Gurson AL. Continuum theory of ductile rupture by void nucleation and growth: Part I—yield criteria and flow rules for porous ductile media. 1977.
[62] Tvergaard V. Influence of voids on shear band instabilities under plane strain conditions. Int J Fract 1981;17:389–407.
[63] Ross CA, Tedesco JW, Kuennen ST. Effects of strain rate on concrete strength. Mater J 1995;92(1):37–47.
[64] Fu H, Erki M, Seckin M. Review of effects of loading rate on concrete in compression. J Struct Eng 1991;117(12):3645–59.
[65] Cusatis G. Strain-rate effects on concrete behavior. Int J Impact Eng 2011;38(4):162–70.
[66] Kong X, Fang Q, Zhang J, Zhang Y. Numerical prediction of dynamic tensile failure in concrete by a corrected strain-rate dependent nonlocal material model. Int J Impact Eng 2020;137:103445.
[67] Nyström U, Gylltoft K. Comparative numerical studies of projectile impacts on plain and steel-fibre reinforced concrete. Int J Impact Eng 2011;38(2–3):95–105.
[68] Luccioni B, Aráoz G. Erosion criteria for frictional materials under blast load. Mec Comput 2011;30(21):1809–31.
[69] Riedel W, Kawai N, Kondo K-i. Numerical assessment for impact strength measurements in concrete materials. Int J Impact Eng 2009;36(2):283–93.
[70] Wang Z, Wu J, Wang J-G. Experimental and numerical analysis on effect of fibre aspect ratio on mechanical properties of srfc. Constr Build Mater 2010;24(4):559–65.
[71] Cadoni E, Labibes K, Albertini C, Berra M, Giangrasso M. Strain-rate effect on the tensile behaviour of concrete at different relative humidity levels. Mater Struct 2001;34(1):21–6. http://dx.doi.org/10.1007/BF02482196.
[72] Vu X, Malecot Y, Daudeville L. Influence of the saturation degree and mix proportions on the behavior of concrete under high level of stresses. In: 6th international conference on fracture mechanics of concrete and concrete structures. Vol. 3, 2007, p. 1815–20.
[73] Accary A. Experimental characterization of the interstitial pore pressure of wet concrete under high confining pressure (Ph.D. thesis), Université Grenoble Alpes; 2018.
[74] Baroth J, Briffaut M, Vu D, Malecot Y, Daudeville L. Prediction of perforation into concrete accounting for saturation ratio influence at high confinement. Int J Impact Eng 2021;156:103923. http://dx.doi.org/10.1016/j.ijimpeng.2021.103923.